Andreev Reflection in the Fractional Quantum Hall State

Önder Gül,[1,†] Yuval Ronen,[1,†] Si Young Lee,[1,2,†] Hassan Shapourian,[1,3] Jonathan Zauberman,[1] Young Hee Lee,[2,4] Kenji Watanabe,[5] Takashi Taniguchi,[6] Ashvin Vishwanath,[1] Amir Yacoby,[1] and Philip Kim[1,*]

[1]*Department of Physics, Harvard University, Cambridge, Massachusetts 02138, USA*
[2]*Center for Integrated Nanostructure Physics (CINAP), Institute for Basic Science (IBS), Suwon 34126, Republic of Korea*
[3]*Department of Physics, Massachusetts Institute of Technology, Cambridge, Massachusetts 02138, USA*
[4]*Department of Energy Science, Sungkyunkwan University, Suwon 16419, Republic of Korea*
[5]*Research Center for Functional Materials, National Institute for Materials Science, Tsukuba 305-0044, Japan*
[6]*International Center for Materials Nanoarchitectonics, National Institute for Materials Science, Tsukuba 305-0044, Japan*

(Received 20 September 2021; accepted 4 May 2022; published 14 June 2022)

We construct high-quality graphene-based van der Waals devices with narrow superconducting niobium nitride (NbN) electrodes, in which superconductivity and a robust fractional quantum Hall (FQH) state coexist. We find a possible signature for crossed Andreev reflection (CAR) across the superconductor separating two FQH edges. Our observed CAR probabilities in the particlelike fractional fillings are markedly higher than those in the integer and hole-conjugate fractional fillings and depend strongly on temperature and magnetic field unlike the other fillings. Further, we find a filling-independent CAR probability in integer fillings, which we attribute to spin-orbit coupling in NbN allowing for Andreev reflection between spin-polarized edges. These results provide a route to realize novel topological superconducting phases in FQH-superconductor hybrid devices based on graphene and NbN.

DOI: 10.1103/PhysRevX.12.021057 Subject Areas: Condensed Matter Physics

I. INTRODUCTION

Topological superconductors are predicted to represent a phase of matter with nonlocal properties, providing a robustness suitable for quantum computing [1–5]. A theoretical proposal to synthesize a topological superconductor from a topological insulator and a conventional (*s*-wave) superconductor has motivated hybrid approaches to realize Majorana modes. Besides topological insulators [6–8], these approaches now include spin-orbit coupled semiconductors [9–14], magnetic atom chains [15], and integer quantum Hall edges [16–19]—all in combination with a superconductor—offering either a test bed for or a route toward topological qubits. Common to all of these is the noninteracting description of charge carriers and Ising topological order which is insufficient for universal quantum computation [4]. These approaches, however, can be extended to the computationally universal Fibonacci order [20] predicted to emerge in a coupled parafermion array [21].

Parafermions, unlike Majoranas, require electron-electron interactions to form, which result in richer non-Abelian braiding statistics [22]. An established condensed matter system that forms with interactions is the fractional quantum Hall (FQH) state, which is the basis of different approaches for synthesizing parafermions [20–29]. The primary approach—combining a FQH state, appearing in semiconductor heterostructures, with superconductivity [21,24–28]—has so far presented two major experimental challenges. First, the strong magnetic fields required for a FQH state suppress superconductivity [16–19,30]. Second, coupling a superconductor to a semiconductor heterostructure [31] can be difficult, often leading to a nontransparent interface. Here, we overcome these challenges by using graphene-based van der Waals (vdW) heterostructures coupled to superconducting niobium nitride (NbN). The high device quality decreases the magnetic fields required for a robust FQH state to the regime where NbN remains superconducting owing to its large critical field. The superconductor edge contact to graphene provides an interface transparent enough to allow Andreev reflection in quantum Hall edges.

*Corresponding author.
philipkim@g.harvard.edu
†These authors contributed equally to this work.

II. DEVICE AND CROSSED ANDREEV REFLECTION IN THE FQH STATE

Figure 1(a) shows the schematic of our vdW heterostructure, consisting of single-layer graphene as the conducting channel, which is first encapsulated by hexagonal boron nitride dielectric and then by graphite on both top and bottom. This heterostructure maximizes the channel mobility owing to the metallic graphite layers screening remote impurities [32,33], which is essential for reaching the FQH phase at magnetic fields low enough to allow superconductivity. Figure 1(b) shows a typical device, including the heterostructure (purple) and a <100-nm-wide NbN superconductor (blue) which is sufficiently narrow (coherence length ~50 nm) [17] to allow the possibility of crossed Andreev reflection (CAR) between the quantum Hall edges on both sides (see also Fig. 6 for the images of the measured devices), a necessary ingredient for realizing parafermions [34]. CAR dramatically affects transport: when the injected electronlike charges are drained from the superconductor, holelike charges propagate away [Fig. 1(c)].

We have measured the resistance $R_{\mathrm{CAR}} = V_{\mathrm{CAR}}/I_{\mathrm{exc}}$ as well as the Hall resistance $R_{XY} = V_{XY}/I_{\mathrm{exc}}$ as a function of gate voltage (charge carrier density) at a magnetic

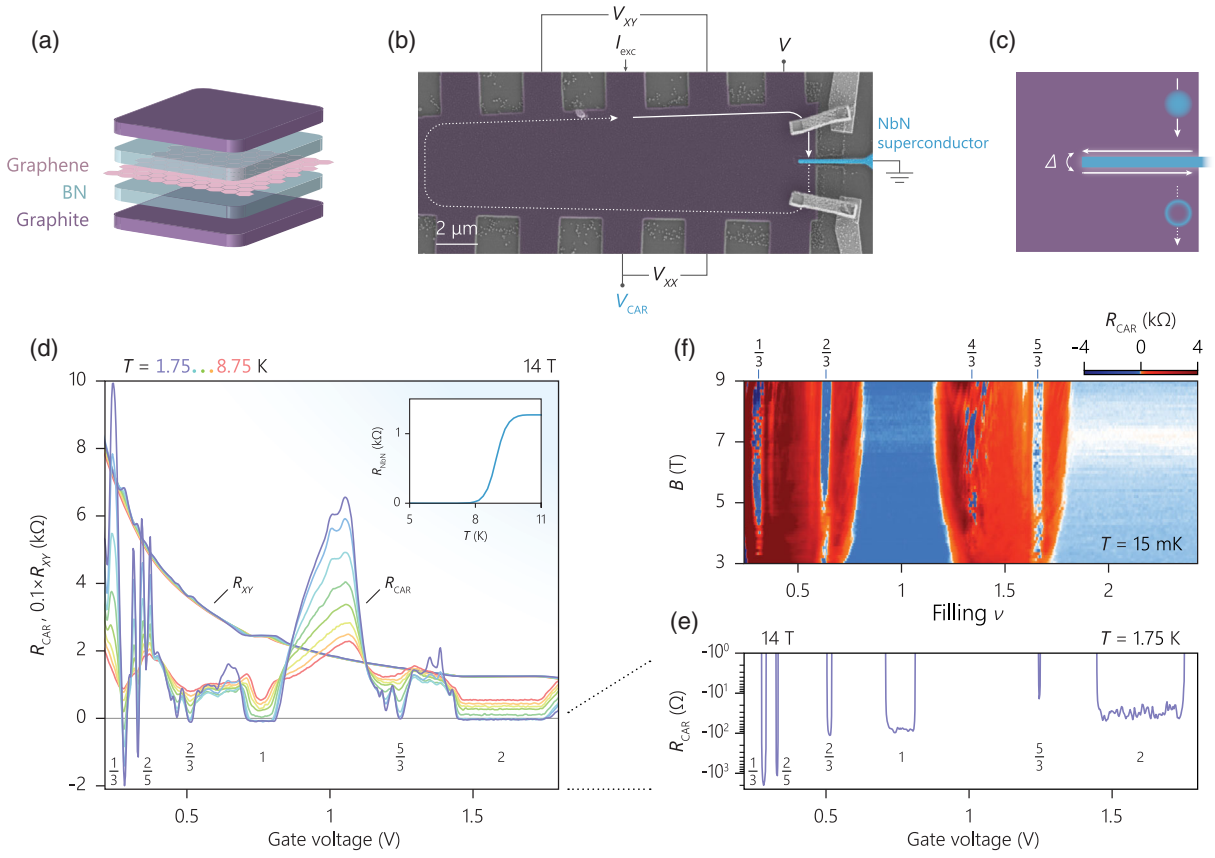

FIG. 1. The device and crossed Andreev reflection (CAR) in a FQH state. (a) Schematic of the heterostructure. Graphene is encapsulated with boron nitride dielectric and graphite. (b) Typical device including a NbN superconductor <100 nm in width and ~1 μm in length (blue). The extended arms connect to normal leads (not shown) that are used to bias a current I_{exc}, measure the voltages V_{XX} and V_{XY}, the potential of the edge mode propagating toward the superconductor V, and finally that of the edge mode propagating away V_{CAR}. The superconductor is grounded, remaining leads are floating. The solid and the dashed arrows depict, respectively, the chiral electron and hole conduction in an out-of-plane magnetic field B. The metal electrodes on top graphite (gate) are bridges that connect the top gate to leads avoiding the edge of the heterostructure. (c) Illustration of the theory model. A narrow superconductor induces a pairing gap Δ between the counterpropagating fractional quantum Hall edges along both sides. Δ converts an incoming electron to an outgoing hole by crossed Andreev reflection. (d) $R_{\mathrm{CAR}} = V_{\mathrm{CAR}}/I_{\mathrm{exc}}$ and $R_{XY} = V_{XY}/I_{\mathrm{exc}}$ as a function of gate voltage measured at $B = 14$ T for different temperatures T. An $R_{\mathrm{CAR}} < 0$ at fractional quantum Hall plateaus indicates hole conductance (CAR). Measured R_{XY} for $\nu < 1$ (high channel impedance) is slightly lower than the expected quantized values, with up to ~10% deviation for $\nu = 1/3$, due to a resulting small low-pass frequency in this experimental setup. Similar signal magnitude reduction is expected for R_{CAR} for $\nu < 1$. This effect does not result in a spurious negative contribution that can increase the negative CAR reading. Inset of (d) shows the resistance of a narrow NbN for varying T which superconducts below 8 K at 14 T. (e) R_{CAR} at 1.75 K from (d). (f) R_{CAR} as a function of filling ν and B measured at 15 mK. CAR ($R_{\mathrm{CAR}} < 0$) is observed at 3 T for $\nu = 2/3$.

field $B = 14$ T for different temperatures T [Fig. 1(d)]. Here, V_{CAR} is the potential of the edge mode propagating away from the grounded superconductor, V_{XY} is the Hall voltage, and I_{exc} is the bias current [see Fig. 1(b) for the circuit]. At low T, R_{CAR} becomes negative for quantized values of R_{XY}. We find an $R_{\mathrm{CAR}} < 0$ for both integer fillings 1 and 2 [17], and importantly for several fractional fillings $1/3, 2/5, 2/3, 5/3$—our main finding [enlargement shown in Fig. 1(e)]. An $R_{\mathrm{CAR}} < 0$ indicates that the electronlike carriers drained from the superconductor produce holelike carriers with opposite charge, a direct result of crossed Andreev reflection, which reverses the sign of the edge potential. R_{CAR} acquires positive values either when R_{XY} is nonquantized and the bulk of the device conducts or when superconductivity is suppressed with increasing T—both destroying CAR as expected. We confirm that our narrow NbN superconducts at 14 T for $T < 8$ K by measuring a strip with identical dimensions as the one coupled to the quantum Hall edges [Fig. 1(d), inset]. In a separate cooldown with T reaching 15 mK, we find $R_{\mathrm{CAR}} < 0$ for several fractional fillings for a wide range of B [Fig. 1(f)]. At this low temperature, CAR in the FQH state can be observed in magnetic fields as low as 3 T (filling $2/3$).

III. SPIN-ORBIT COUPLING (SOC)

Figure 2(a) shows R_{CAR} with the accompanying longitudinal resistance R_{XX} as a function of filling ν. For all integer fillings R_{XX}, which measures bulk conduction, is much smaller in amplitude than R_{CAR}, linking R_{CAR} strictly to the potential of the edge mode leaving the superconductor. We find a negative edge potential with consistently increasing amplitude for lower fillings, which remains negative for all integer ν and measured B demonstrating the robustness of CAR [Fig. 2(a), inset].

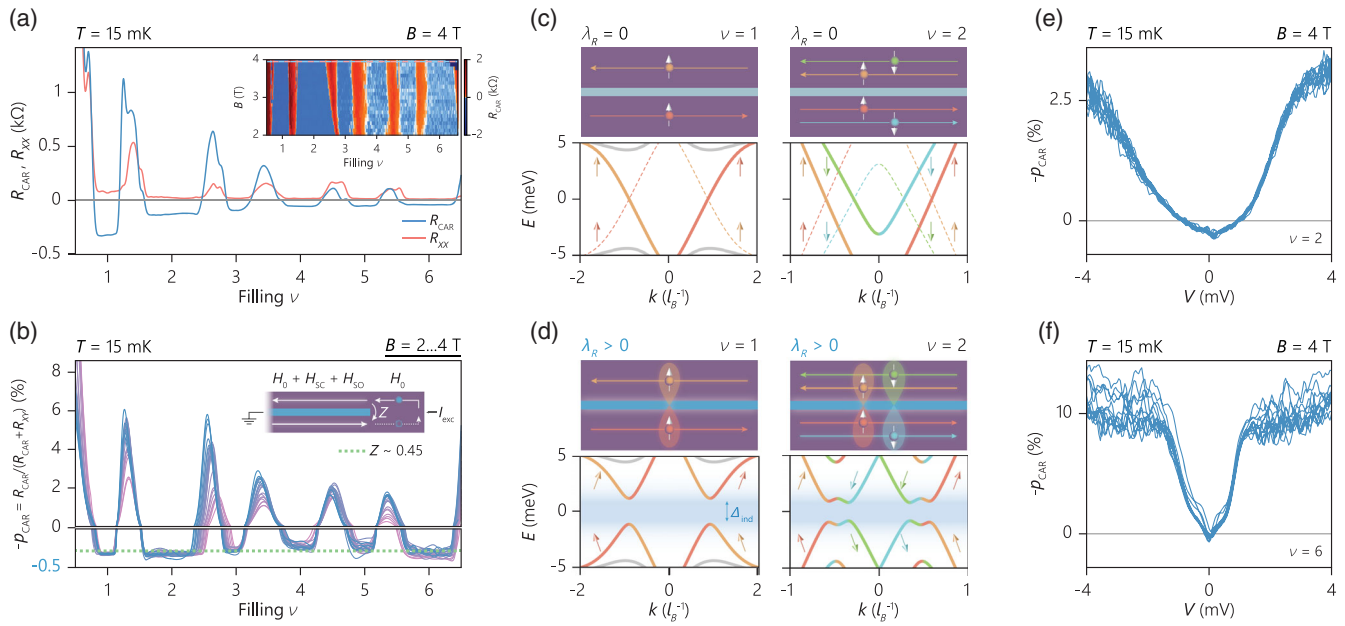

FIG. 2. Spin-orbit coupling. (a) R_{CAR} and R_{XX} as a function of filling ν. All integer ν show crossed Andreev reflection ($R_{\mathrm{CAR}} < 0$). Small R_{XX} indicates negligible bulk conductance. Inset of (a) shows R_{CAR} measured at $B = 2, \ldots, 4$ T. (b) CAR probability p_{CAR} of the inset of (a). All integer ν, including the spin-polarized $\nu = 1$, have a comparable p_{CAR}, an evidence for the pairing mechanism being the same for all integer ν, enabled by spin-orbit coupling. The dashed line is the average p_{CAR}. H_0 is the Hamiltonian of the edges, H_{SC} the pairing, and H_{SO} the spin-orbit Hamiltonian. Z represents incoming charges tunneling to the outgoing edge mode without Andreev reflection (direct tunneling). (c) Illustration of the edges separated by a superconductor without spin-orbit coupling ($\lambda_R = 0$) for $\nu = 1$, 2, and their calculated Bogoliubov–de Gennes spectrum. No pairing gap is present ($\Delta_{\mathrm{ind}} = 0$). Momentum k in units of l_B^{-1} with l_B the magnetic length. Solid lines are the electronlike excitations, dashed lines the holelike. Color code indicates the spin and the direction of propagation. (d) Inclusion of spin-orbit coupling tilts the spins and enables a pairing gap Δ_{ind}. The only possible pairing is p wave for any integer ν irrespective of whether it is spin polarized or not. The inner edge modes pair more strongly due to their proximity to the superconductor. However, for low energy and temperature, p_{CAR} is expected to be independent of the size of Δ_{ind}. Here, the value of λ_R is chosen to provide a spectral superconducting gap matching the experimentally relevant Δ_{ind} (see Supplemental Material, Table S3 [35]). (e) p_{CAR} at $\nu = 2$ as a function of the incoming edge mode potential V (excitation) for different gate voltages spanning the entire QH plateau region. Crossed Andreev reflection is limited to below $|eV| \sim 1$ meV. (f) Same as (e) but at $\nu = 6$. CAR is observed for $|eV| < 0.2$ meV.

The increasing amplitude of R_{CAR} with decreasing ν is connected to the decreasing number of edge modes, which increases R_{XY}. This dependence of R_{CAR} on ν can be understood by introducing $p_{\mathrm{CAR}} = -V_{\mathrm{CAR}}/V$, the probability of crossed Andreev reflection, where V is the potential of the incoming edge mode. The Hall voltage constrains $V_{XY} = V - V_{\mathrm{CAR}}$, leading to the proportional relation $R_{\mathrm{CAR}} = -R_{XY}/(1 + p_{\mathrm{CAR}}^{-1})$. This allows us to calculate p_{CAR} from the measured R_{CAR}, and thus to directly compare the CAR rate between different fillings. Figure 2(b) shows that p_{CAR} is comparable for all integer ν, including the spin-polarized $\nu = 1$. This striking finding provides evidence for the presence of strong spin-orbit coupling (SOC) in the NbN superconductor. Without this SOC, CAR cannot occur in the spin-polarized edges due to the s-wave superconducting pairing in NbN. Our Bogoliubov–de Gennes spectrum, calculated for integer $1 \leq \nu \leq 6$, supports this observation [Figs. 7 and 17; see also Fig. 2(b), inset, Appendix B, and Supplemental Material for the theory model [35]]. Figures 2(c) and 2(d) show the energy spectrum of $\nu = 1$ and 2 without and with SOC, represented in our Hamiltonian by the term λ_R. A pairing gap Δ_{ind} does not open without SOC [Fig. 2(c)]. The inclusion of SOC allows for pairing ($\Delta_{\mathrm{ind}} > 0$) between the two counterpropagating spin-up edges of $\nu = 1$, and separately between the two additional counterpropagating spin-down edges of $\nu = 2$ [Fig. 2(d)]—pairing between the edges with opposite spin polarization is forbidden owing to the difference in their Fermi wave vector k_F. Interestingly, our comparable p_{CAR} for all integer ν and its magnetic field insensitivity for small I_{exc} and T (compared to Δ_{ind}) is consistent with a topologically nontrivial Δ_{ind}.

Our p_{CAR} remains much smaller than unity [36] because of dissipation (subgap transport due to vortices expected for our type-II superconductor) as well as direct tunneling of incoming charges to outgoing edge modes without Andreev reflection. Direct tunneling is microscopically related to disorder in the graphene-superconductor interface, which we effectively model with disordered pairing [37] (see CAR resistance in Supplemental Material [35] and Figs. 18 and 19). Our model does not include edge reconstruction [38] or charge accumulation at the superconductor interface (both discussed below) but accounts for Andreev edge states demonstrated in quantum Hall–superconductor hybrids without counterpropagating edge modes [16,18,19,30,39,40]. Andreev edge states do not result in a pairing gap (Fig. 17) and in a graphene-based device produce a response sensitive to small changes in gate voltage, magnetic field, and the length of the superconductor interface, which averages to zero [18]. In contrast, our CAR response is robust, consistently negative, and independent of the interface length (Fig. 6), suggesting an induced pairing. We note that Ref. [19] finds consistently negative CAR response in InAs-based devices in a geometry excluding counterpropagating edge modes and supporting Andreev edge states.

A potential link between CAR and the induced pairing may also be revealed by spectroscopy. We have varied the energy of the injected charges by tuning V, serving as the bias voltage [Fig. 1(b)], and found CAR to be limited to low energies [Figs. 2(e) and 2(f)]. Notably, the energy range of CAR in $\nu = 2$ is larger than in $\nu = 6$, consistent with a larger pairing gap for lower fillings owing to their edge modes' closer proximity to the superconductor (Fig. 19). This gate dependence excludes, for integer fillings, the effects of nonproximitized residual edge modes originating from the work function mismatch between the graphene channel and the superconductor, which would result in ν-independent spectroscopic properties. (A work function mismatch tends to produce a heavily doped region near the contact [41], whose precise physical extent in our device cannot be measured directly.)

IV. MAGNETIC FIELD DEPENDENCE

We now extend our analysis of p_{CAR} to fractional ν and a larger B range. Figure 3(a) shows p_{CAR} and the accompanying νR_{XX} (R_{XX} normalized for different ν), with the measured R_{CAR} and R_{XX} at $B = 9$ T plotted in Fig. 3(b). For all fractional ν with $R_{\mathrm{CAR}} < 0$, we find a negligibly small R_{XX} which excludes bulk conduction. Bulk conduction does, however, result in $R_{\mathrm{CAR}} > 0$ observed for lower values of B or for fractional ν with smaller excitation gaps. Figure 3(c) shows the B dependence of p_{CAR} for several fractional and integer ν. In this B range, we again find for several fillings a p_{CAR} that does not depend on B and is comparable between different ν, this time including several fractional ν [Fig. 3(b), inset]. Importantly, this observation is contrasted by particlelike fillings $\nu = 1/3$ and $4/3$, which present a well-developed FQH state (negligible R_{XX}) together with a strong magnetic field dependence. The origin of this behavior is presently unknown and can be either a result of edge reconstruction or intrinsic to the superconducting pairing of FQH edges. Identifying these scenarios theoretically is challenging due to the interacting many-body nature of a FQH state not allowing for our Bogoliubov-Dirac-Landau analysis. Experimentally, we find a p_{CAR} that strongly depends on B (and T, presented below) only for the particlelike FQH states whose p_{CAR} is significantly larger than that for integer ν. Such B and T dependences are much weaker for $\nu = 2/3$ and $5/3$, as well as for the FQH states in our second device—although with a slightly different geometry and measured at higher $T > 1.6$ K—whose p_{CAR} are comparable to those for integer states (Figs. 4,8–14).

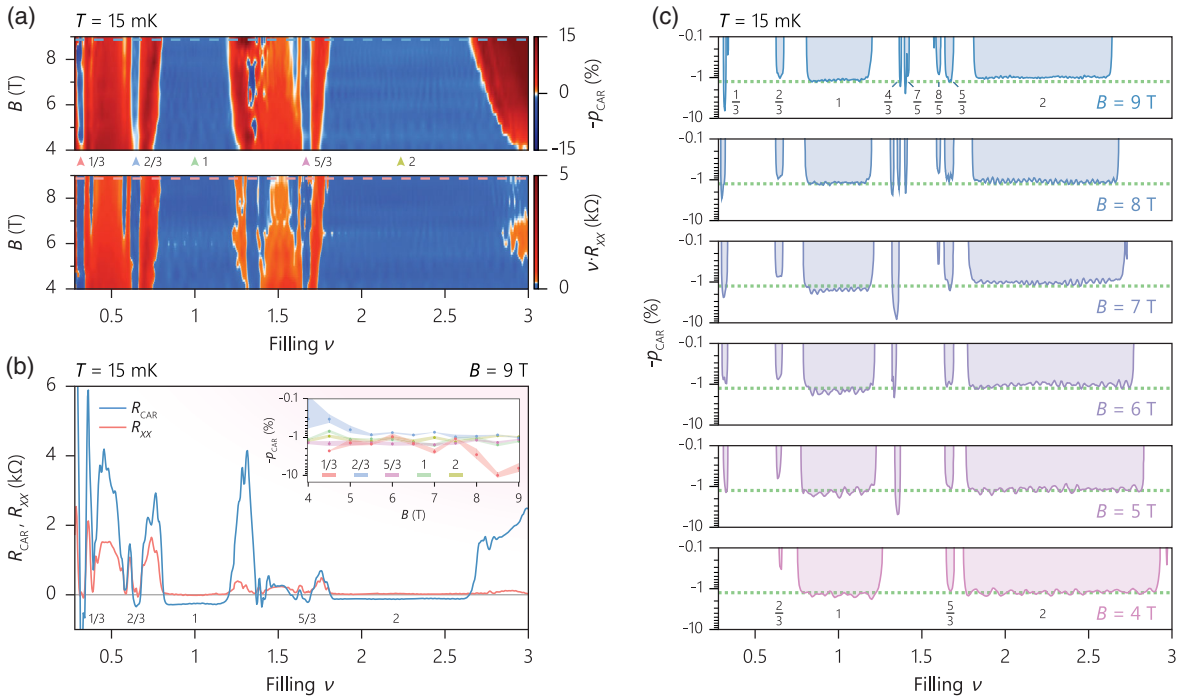

FIG. 3. Magnetic field dependence. (a) p_{CAR} and R_{XX} (normalized for different ν) as a function of filling and magnetic field B. These measurements have a step size of 0.5 T and have been interpolated in B axis corresponding to 0.1 T steps in order to provide visibility for the evolution of the conductance features in magnetic field. (b) R_{CAR} and R_{XX} at $B = 9$ T from (a). Small R_{XX} indicates negligible bulk conductance. Inset of (b) shows p_{CAR} from (a) as function of B for several ν. p_{CAR} of $\nu = 1/3$ shows a strong B dependence reaching 10% at $B = 8.5$ T. $p_{\mathrm{CAR}} \sim 1\%$ for the rest of the fillings shown. The shades represent the uncertainty in the measured values. (c) p_{CAR} from (a) for $B = 4, \ldots, 9$ T. p_{CAR} at $\nu = 1/3$ and $4/3$ changes with B, reaching, respectively, >6% ($B = 9$ T) and >8% ($B = 7$ T). The rest of the fillings are insensitive to B once they are well developed. The dashed line is the average p_{CAR} for fillings which do not exhibit a B dependence.

V. GRAPHENE REGION SURROUNDING THE SUPERCONDUCTOR

To investigate the pronounced CAR of particlelike fractions, we simultaneously control top and bottom gate voltage in our second device, which allows for tuning the density in the ∼100 nm narrow graphene region surrounding the superconductor without affecting the bulk filling ν [Fig. 4(a)]. This experimental knob affects the filling ν' around the superconductor, which enables the probing of the profiles of the FQH edges and the extent of charge accumulation at the superconductor interface (contact-induced doping). Varying ν' for constant ν changes the existing edge modes along the superconductor, as shown in Fig. 4(b) for the depleted, neutral (ν' matches ν) and accumulated narrow graphene region. First, we observe that the particlelike fractional states $\nu = 1/3$, $2/5$ [Fig. 4(c)] produce a qualitatively different behavior from the integer [Fig. 4(e)] or hole-conjugate fractional states $\nu = 3/5$, $2/3$ [Fig. 4(d)]: while CAR in the particlelike fractions is limited to the matched regime, CAR in the integers or hole-conjugate fractions is not suppressed in the accumulation regime. This could be related to the details of edge profile and reconstruction in, for instance, $\nu = 1/3$ and $2/3$, where $1/3$ is described by a single edge mode whereas $2/3$ is described by counterpropagating edge modes of 1 and $1/3$ which equilibrate [42,43]. Second, for all FQH states a small decrease of ν' compared to ν suppresses CAR. These observations are compatible with the scenario that the accumulation region in the graphene channel related to contact-induced doping is very narrow (≪100 nm) and thus fully proximitized, which can potentially explain the strong CAR response for particlelike FQH edges. However, we cannot rule out alternative explanations such as a mundane disorder-induced origin for our pronounced CAR in certain fractions.

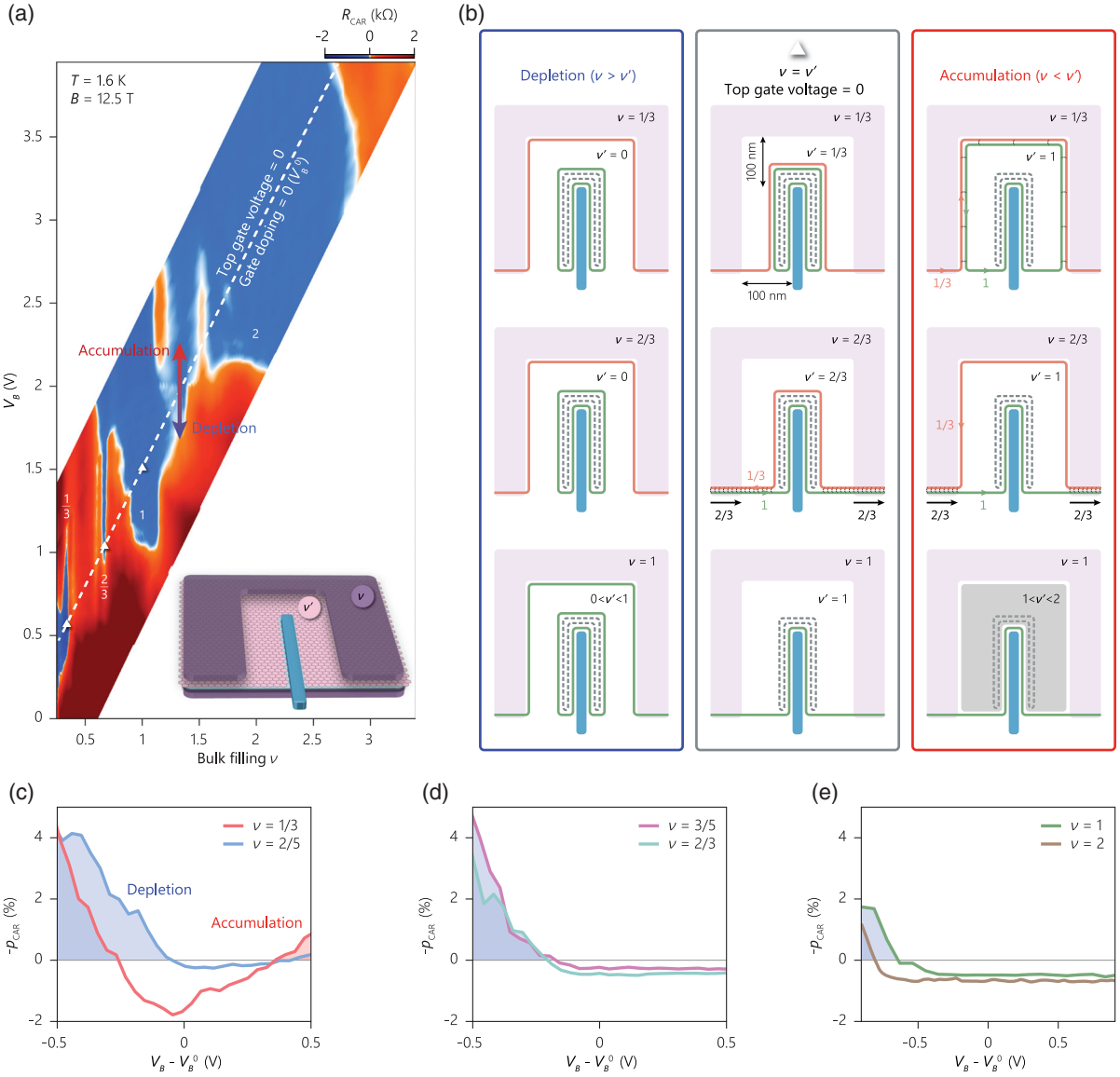

FIG. 4. Graphene region surrounding the superconductor. (a) Inset illustrates the region around the superconductor in our devices. The ∼100 nm narrow graphene region surrounding the superconductor is not covered by top graphite (gate). This enables tuning the density (filling ν') around the superconductor without affecting the bulk filling ν. Here, ν is set simultaneously by top and bottom gate: $\nu \propto (V_T + c \cdot V_B)$ where V_T is the top gate voltage, V_B the bottom, and $c = 0.51$ the ratio of the capacitive couplings of top and bottom gate to the bulk graphene. In contrast, graphene surrounding the superconductor is capacitively coupled primarily to the bottom gate ($\nu' \propto V_B$). Color plot shows CAR for several fillings ν as a function of V_B. The symbols mark the edge mode configurations illustrated in (b) corresponding to the matched ($\nu = \nu'$) regime for which $V_T = 0$. Increasing V_B results in the accumulation ($\nu < \nu'$) regime, whereas decreasing V_B results in the depletion ($\nu > \nu'$) regime. The dashed line marks V_B^0, the value of V_B for which $V_T = 0$. (b) Illustrations of the edge mode configuration of the particlelike $\nu = 1/3$, the hole conjugate $\nu = 2/3$, and the integer $\nu = 1$ for varying ν'. The dashed and the solid green line surrounding the superconductor illustrate integer edge modes potentially induced by an increased charge carrier density at the superconductor interface (contact-induced doping). The thin dashed arcs between the two edge modes 1/3 (orange line) and 1 (green line) depict their equilibration with each other. CAR is absent in the depletion regime, present in the matched regime. Our observed suppression of CAR in $\nu = 1/3$ for $\nu' = 1$ suggests an incomplete equilibration between the edge modes 1/3 and 1 along the electrostatically defined edge (accumulation, top panel). In contrast, CAR in $\nu = 2/3$ is present for $\nu' = 1$, which is consistent with a complete equilibration between the two edge modes along the physical sample edge (accumulation, middle panel). Shaded area in the bottom right accumulation panel depicts a compressible region. The presence of CAR for this filling configuration ($\nu = 1 < \nu'$) suggests negligible tunneling between the edge mode and the compressible region. We also note that we did not observe oscillatory conductance between the two fillings 1/3 and 1, presumably due to the 1D nature of the interface between them and higher temperatures than in the recent experiment [44]. (c) CAR in the particlelike fractional states is limited to small $|V_B - V_B^0|$. (d),(e) CAR in the integer and the hole-conjugate fractional states are not suppressed for large $V_B - V_B^0$.

VI. TRANSPORT SPECTROSCOPY AND TEMPERATURE DEPENDENCE

Next, we perform spectroscopy in fractional ν by varying V and monitoring p_{CAR} and R_{XX} simultaneously at different temperatures. Figures 5(a)–5(d) show CAR for $\nu = 1/3$ and $2/5$, both limited to an energy range below $|\mathrm{eV}| \sim 1$ meV and to low T (see also the color plots as insets and Fig. 15, which shows R_{CAR} instead of p_{CAR}). Increasing V and T bring the injected charges above the excitation gap of the fractional fillings (bulk conduction) or above Δ_{ind} (Bogoliubov-quasiparticle transport without Andreev reflection), both suppressing CAR. The comparison of fractional ν (excitation gaps in the same range as Δ_{ind}) with $\nu = 2$ (largest Landau gap, significantly larger than Δ_{ind}) suggests that for our fractional ν an increasing V suppresses CAR primarily due to bulk conduction, while the suppression with T is due to both bulk conduction and Bogoliubov-quasiparticle transport [Figs. 5(a) and 5(c) versus Figs. 5(a), left-hand inset; Figs. 5(b) and 5(d) versus Fig. 14].

We proceed with the temperature dependence of p_{CAR} for several integer and fractional ν [Fig. 5(e)]. We find consistent CAR below $\sim$5 K for all well-developed fillings, demonstrating the robustness of superconductivity in the FQH state. Above this T increasing quasiparticle transport overcomes CAR. The CAR at $\nu = 1$ and 2 persists up to a larger T in our second device measured using a different setup (Fig. 14), indicating that quasiparticle transport can be further decreased.

Figure 5(f) shows the vertical cuts from Fig. 5(e) for several ν. We find a p_{CAR} saturating at low temperatures for the integer fillings $\nu = 1$, 2 as well as $\nu = 2/3$. Interestingly, a topological Δ_{ind} is also expected to provide a temperature-independent behavior for integer ν, equivalent to the B independence presented in Figs. 2 and 3. In stark contrast, the particlelike fillings $\nu = 1/3$ and $2/5$ show a clear temperature dependence down to the lowest T (Fig. 16), with the p_{CAR} of $\nu = 1/3$ reaching above 6% at $T = 15$ mK, as shown in Fig. 3 ($B = 9$ T).

An increasing p_{CAR} with decreasing T could be a feature of the superconducting pairing of fractional charges $e*$ [Fig. 5(f), right-hand inset, and Fig. 20]. Here, considering $\nu = 1/3$, CAR converts an incoming electronlike $e* = 1/3$ to an outgoing holelike $-e* = -1/3$ adding a $2/3$ charge to the superconductor. Such T dependence is not expected for pairing of integer charges in FQH edges [Fig. 5(f), left-hand inset], where, for $\nu = 1/3$, three incoming $e*$ bunch together, which are then converted to three bunched $-e*$ leaving the superconductor. In this case, CAR vanishes ($R_{\mathrm{CAR}} = 0$) at zero temperature, which is not observed for both our devices at our lowest T. Although our experiments do not constitute direct evidence for pairing of fractional charges, which can be complicated by contact-induced doping, our p_{CAR} for fully developed particlelike FQH states being larger than that of integer and hole-conjugate fractional ν suggests a different underlying mechanism for pronounced fractional CAR. Direct evidence for fractional charge pairing could be obtained in measurements which are sensitive to the charge of the Andreev-reflected particles. Additionally, strong bulk disorder in the NbN superconductor corresponding to a mean free path <1 nm, which is smaller than the magnetic lengths $\sim$10 nm in our B range, is expected to result in momentum-nonconserving processes. While such processes should provide an additional s-wave pairing for fillings $\nu \geq 2$, our experiments did not resolve an s-wave contribution which would result in different magnetic field dependence for $\nu = 1$ versus larger fillings $\nu \geq 2$. This is surprising because such strong disorder strengths are expected to suppress p-wave pairing and leave s-wave pairing as the sole mechanism responsible for superconductivity.

Our presented experiments show Andreev reflection in the fractional quantum Hall state, enabled by spin-orbit coupling in the superconductor. Following experiments, including tunneling [29,47], noise [48,49], and supercurrent [50] measurements, will be able to reveal direct evidence for pairing of fractional charges in this hybrid system. Accessing the topological properties will require significant increase of CAR probability by a suppression of edge disorder and vortices, both challenging to be theoretically accounted for in order to predict the experiment, such as temperature dependence.

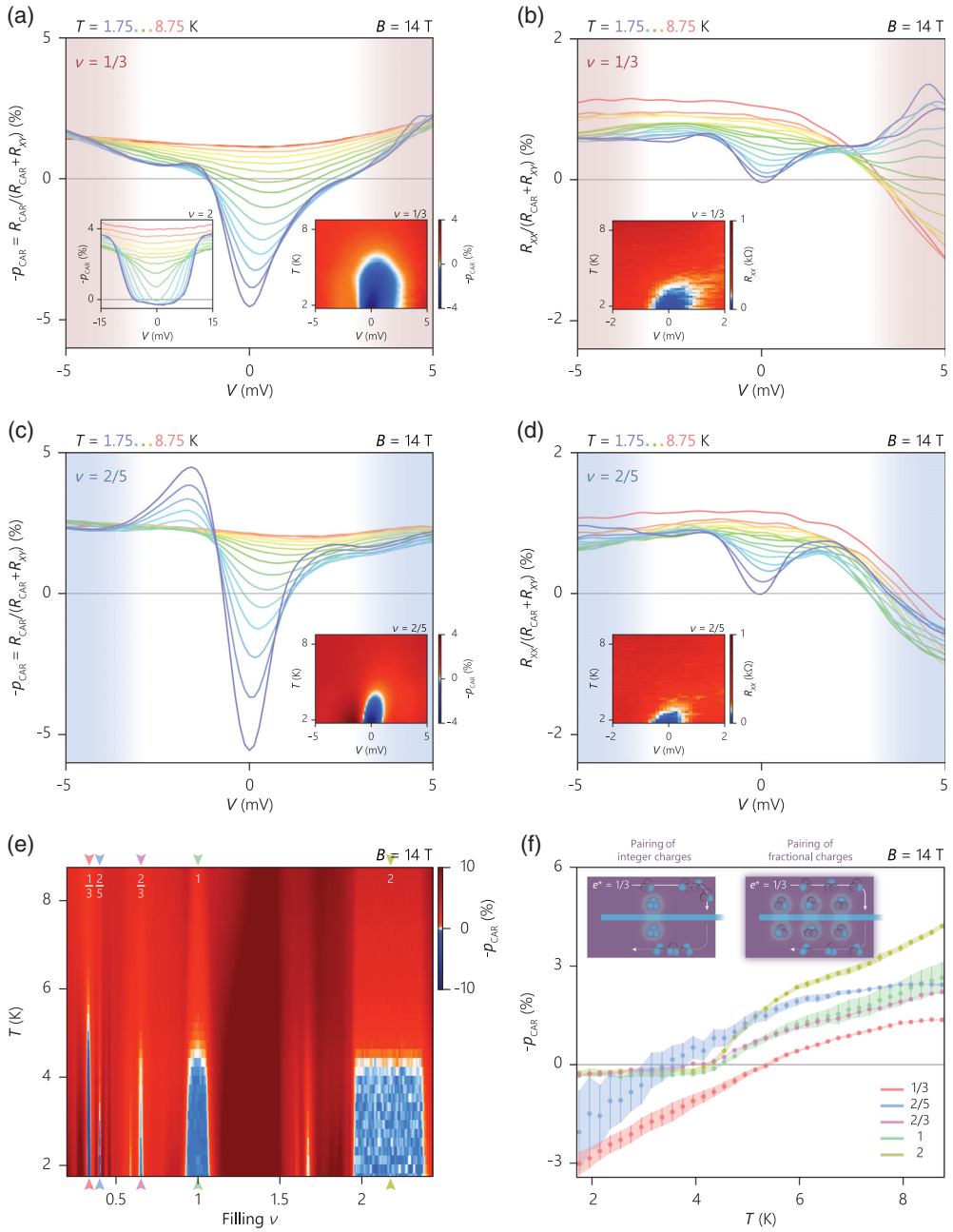

FIG. 5. Transport spectroscopy and temperature dependence. (a) p_{CAR} at $\nu = 1/3$ as a function of the incoming edge mode potential V (excitation) for different temperatures T. Crossed Andreev reflection is limited to below $|eV| \sim 1$ meV and $T < 6$ K. Increasing excitation and T suppress CAR. Left-hand inset of (a) shows p_{CAR} at $\nu = 2$ with a V and T dependence similar to that at $\nu = 1/3$ apart from a larger V range and a smaller p_{CAR}. Right-hand inset of (a) shows the p_{CAR} corresponding to (a). (b) R_{XX} corresponding to (a), divided by the incoming edge mode potential $R_{\mathrm{CAR}} + R_{XY}$, allowing a direct comparison to p_{CAR}. Increasing excitation and T result in bulk conductance which suppresses CAR. Inset of (b) shows R_{XX} corresponding to the right-hand inset of (a). (c),(d) Same as (a) and (b) but for $\nu = 2/5$, which shows a V and T dependence similar to that for $\nu = 1/3$. (e) p_{CAR} as a function of ν for varying T. $R_{\mathrm{CAR}} < 0$ below ~5 K for all well-developed fillings (highlighted with arrows). (f) Vertical cuts from (e). At $\nu = 2/3$, 1, and 2. p_{CAR} saturates below ~4 K with decreasing T, whereas at $\nu = 1/3$ and $2/5$ continues to increase in amplitude without saturating. The shades are the uncertainty in the measurement while sweeping the gate voltage. The uncertainty is larger for fillings represented by fewer data points. Insets of (f) illustrate two different mechanisms of charge transport to the superconductor. Left-hand schematic illustrates bunching of fractional charges of $e* = 1/3$ to form integer charges of e that pair. This mechanism converts three incoming $e*$ to an outgoing $-e$, an integer-charged hole, adding $2e$ to the superconductor. Right-hand schematic illustrates the pairing of fractional charges, a mechanism that converts $e*$ to $-e*$, adding $2e/3$ to a fractional topological superconductor. For pairing of integer charges, p_{CAR} vanishes at $T = 0$. In contrast, p_{CAR} monotonically increases in amplitude with decreasing T when fractional charges pair.

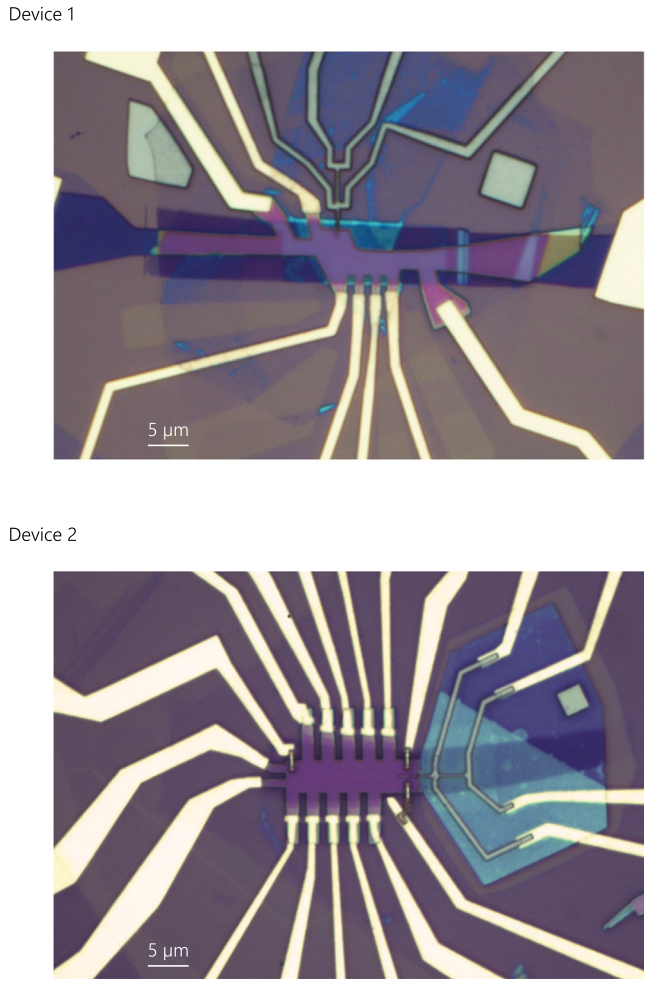

FIG. 6. The presented devices. Data presented in Figs. 1–3,5,15,16 are taken from device 1; Figs. 4,8–14 are taken on device 2. The superconductor in device 1 is ∼1 μm long resulting in a ∼2-μm-long graphene-superconductor interface. The superconductor in device 2 is ∼2 μm long, which results in a ∼4-μm-long interface. No systematic dependence of p_{CAR} on the interface length has been observed. The width of the superconductor is <100 nm in both devices.

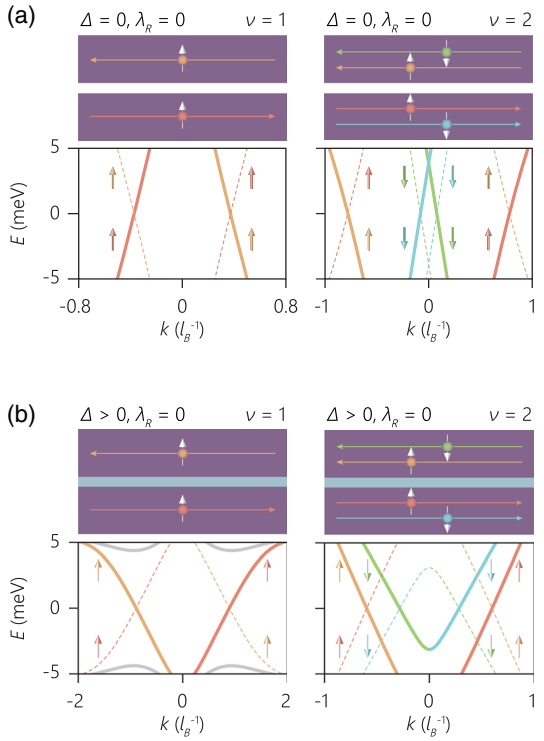

FIG. 7. Evolution of Bogoliubov–de Gennes spectrum when including superconductivity without spin-orbit coupling. (a) Illustration of the edges separated by vacuum for $\nu = 1, 2$, and their calculated Bogoliubov–de Gennes spectrum. Momentum k in units of l_B^{-1} with l_B the magnetic length. k to $-k$ symmetry is a result of physical (Z_2) symmetry—a reflection with respect to the separating vacuum [or superconductor for (b)], which exchanges the left mover and the right mover. Spectrum is doubled to show both electronlike (solid lines) and holelike (dashed lines) excitations. Color code indicates the spin and the direction of propagation. (b) Inclusion of superconductivity ($\Delta > 0$) without spin-orbit coupling ($\lambda_R = 0$) does not affect the spin polarization. This leaves the zero-energy crossings spin polarized, which cannot be gapped by an s-wave superconductor—an induced pairing gap Δ_{ind} does not open. (b) Same as Fig. 2(c). For these simulations and the ones presented in Fig. 2, the system parameters are set as follows: $\Delta_1 = 0.3\varepsilon_0$, $\Delta_2 = 0.2\varepsilon_0$ ($\Delta_{1,2} = 0$ for vacuum), $m_s = 3\varepsilon_0$, $m_n = 0.06\varepsilon_0$, $\mu_s = 8\varepsilon_0$ ($\mu_s = 0$ for vacuum), $\mu_n = 0.2\varepsilon_0$ (for $\nu = 1$), $\mu_n = 0.45\varepsilon_0$ (for $\nu = 2$), $g_n = 0.2\varepsilon_0$, $\lambda_{Ry} = \lambda_{SO} = 0$ and $\lambda_{Rx} = 0.2\varepsilon_0$ ($\lambda_{Rx} = 0$ for no spin orbit), $W_s = 6l_B = 1.7\xi_0 = 62.7$ nm, $\varepsilon_0 = 89$ meV.

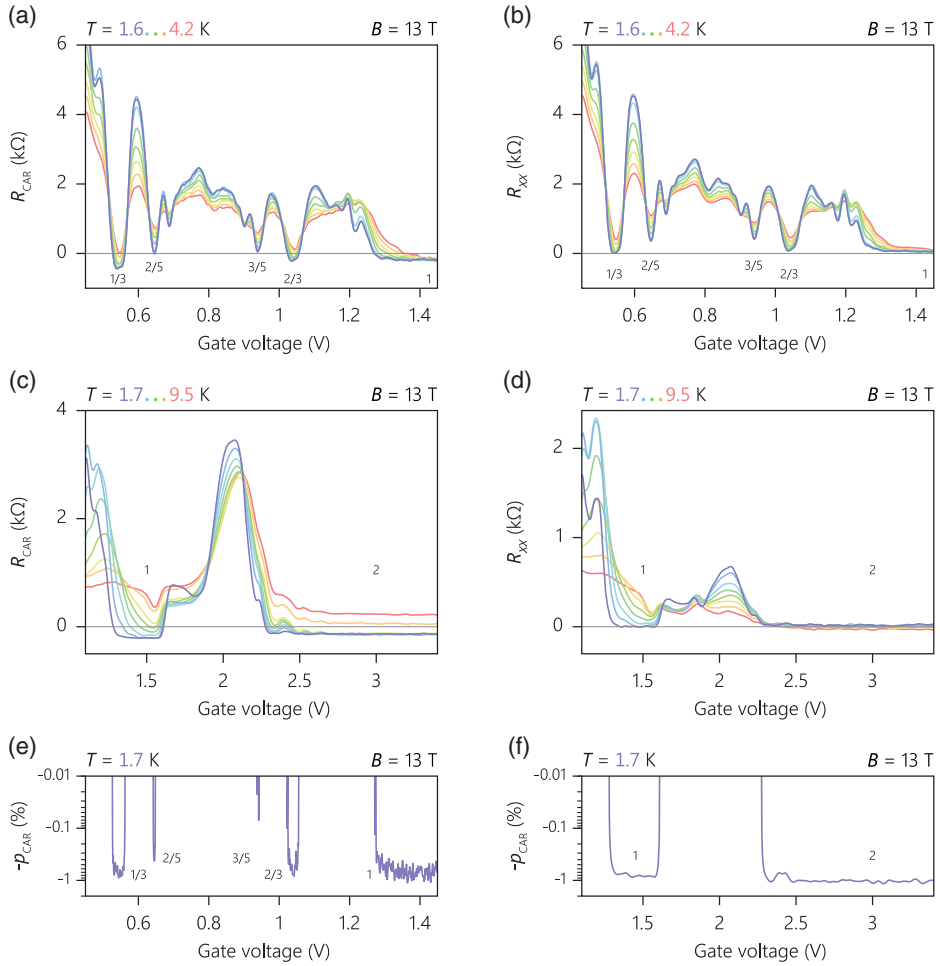

FIG. 8. Crossed Andreev reflection in the FQH state in device 2. (a),(b) R_{CAR} and R_{XX} as a function of gate voltage at $B = 13$ T for different temperatures T. $R_{\mathrm{CAR}} < 0$ at the highlighted fillings indicates crossed Andreev reflection. (c),(d) Same as (a) and (b) but for integer fillings 1 and 2 in a larger T range. (e),(f) p_{CAR} at $T = 1.7$ K, respectively, from (a) and (c).

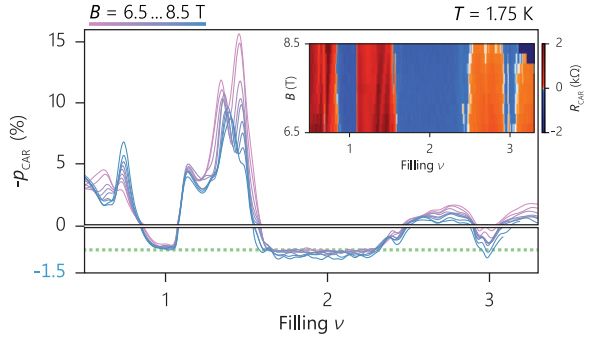

FIG. 9. Spin-orbit coupling in device 2. (a) p_{CAR} as a function of filling ν. Integer fillings, including the spin-polarized $\nu = 1$, have a comparable p_{CAR}, an evidence for the pairing mechanism enabled by spin-orbit coupling. The dashed line is the average p_{CAR}. Inset shows R_{CAR} measured at $B = 6.5, \ldots, 8.5$ T. The filling axis has been adjusted such that the measured fillings align with the integer values of the axis. This procedure to convert gate voltage to filling is present herein and in Figs. 2(a) and 2(b).

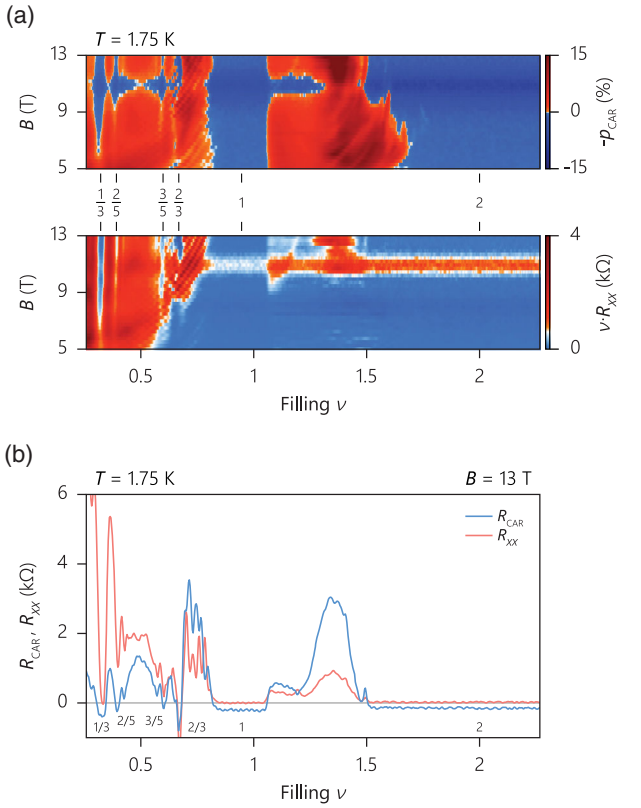

FIG. 10. Magnetic field dependence in device 2. (a) p_{CAR} and R_{XX} (normalized for different ν) as a function of filling and magnetic field B. Crossed Andreev reflection ($R_{\mathrm{CAR}} < 0$) is seen for all well-developed ν. Bulk conduction suppresses CAR observed for lower values of B or for fractional ν with smaller excitation gaps. (b) R_{CAR} and R_{XX} at $B = 13$ T from (a). Bulk conductance (R_{XX}) is negligible for all highlighted fillings except $\nu = 2/3$, a complication related to equilibration in the contact, which is limited to this measurement.

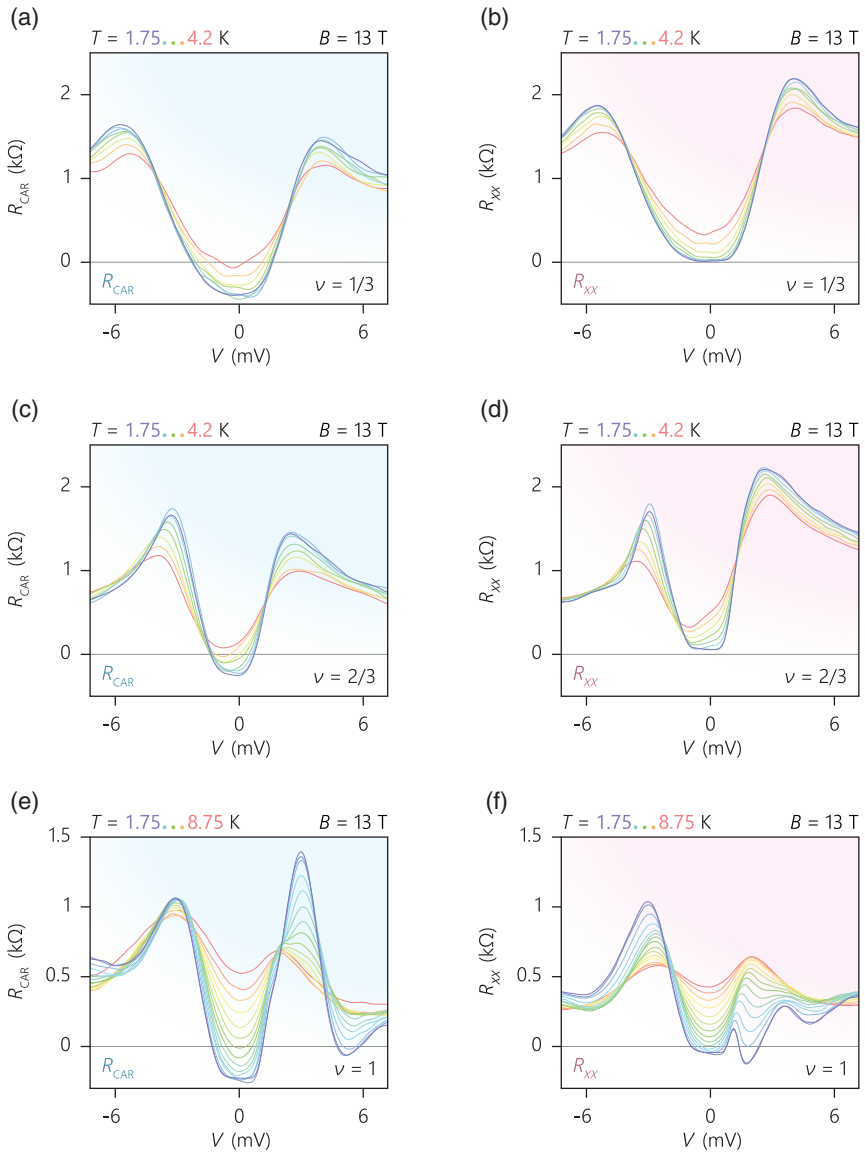

FIG. 11. Transport spectroscopy in device 2 (part 1). (a)–(f) R_{CAR} and R_{XX} at several fillings as a function of the incoming edge mode potential V (excitation) for different temperatures T. Crossed Andreev reflection ($R_{\mathrm{CAR}} < 0$) is limited to below $|eV| \sim 1$ meV. Increasing excitation and T suppress CAR by increasing bulk conductance for these fillings in this device. The features in (e) and (f) appearing at $V \sim 1$ mV correspond to the magnon excitation [45,46], missing in other integer and fractional quantum Hall states.

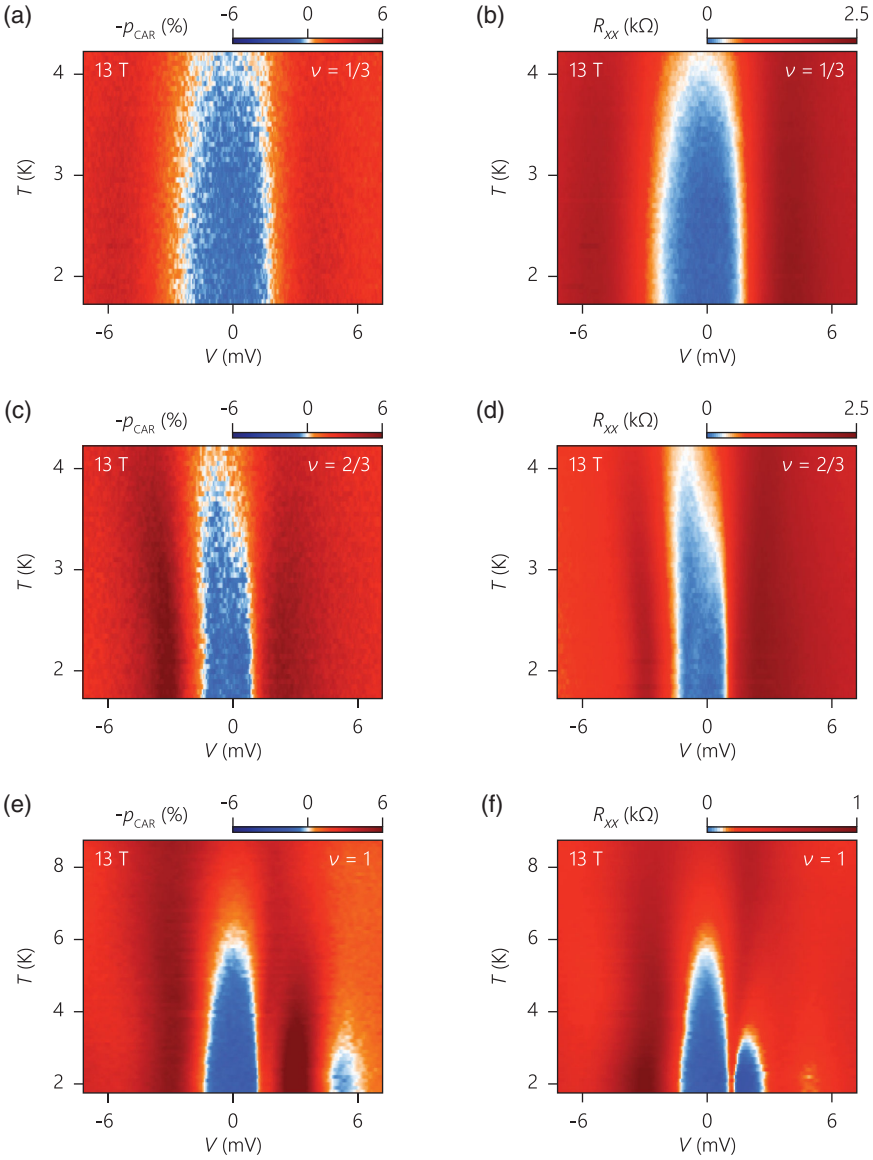

FIG. 12. Transport spectroscopy in device 2 (part 2). (a)–(f) p_{CAR} and R_{XX} at several fillings as a function of the incoming edge mode potential V (excitation) for different temperatures T. Crossed Andreev reflection ($R_{\mathrm{CAR}} < 0$) is limited to below $|eV| \sim 1$ meV, $T \sim 4$ K for $\nu = 1/3$ and $2/3$, and $T \sim 6$ K for $\nu = 1$.

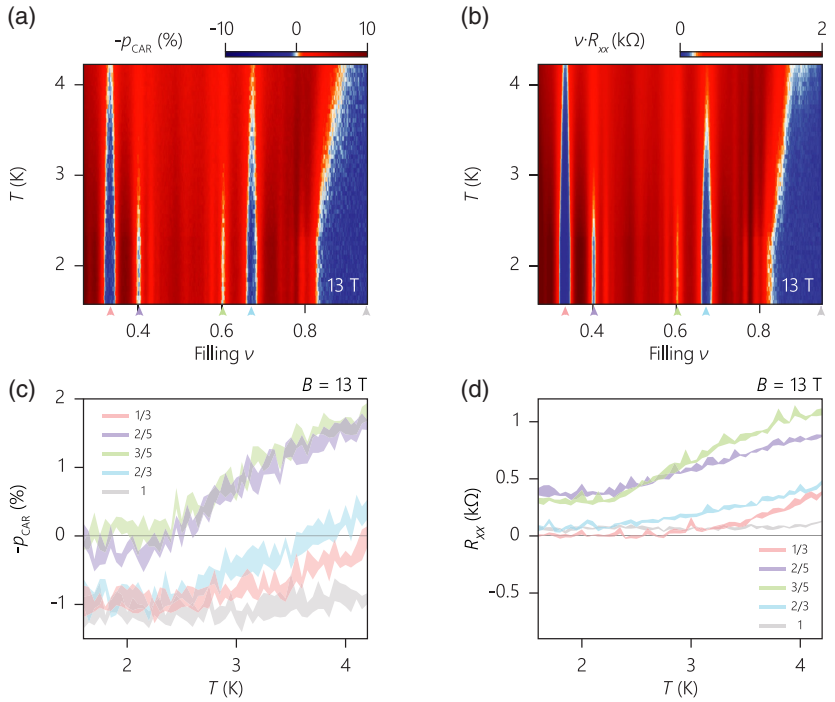

FIG. 13. Temperature dependence in device 2 (part 1, fractional fillings). (a),(b) p_{CAR} and R_{XX} (normalized for different ν) as a function of filling for varying T. Crossed Andreev reflection ($p_{\mathrm{CAR}} > 0$) is seen for the well-developed fillings $\nu = 1/3$, $2/3$, and 1, as well as the fillings with smaller excitation gaps $\nu = 2/5$ and $3/5$, all highlighted with arrows. (c),(d) Vertical cuts, respectively, from (a) and (b). The shades represent the standard deviation.

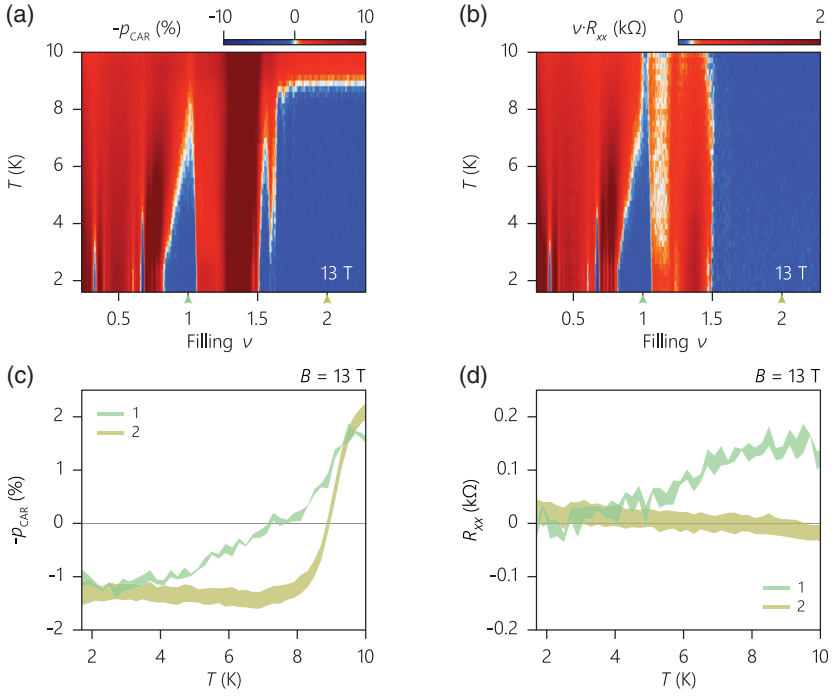

FIG. 14. Temperature dependence in device 2 (part 2, integer fillings). (a),(b) p_{CAR} and R_{XX} (normalized for different ν) as a function of filling for varying T. Crossed Andreev reflection ($p_{\mathrm{CAR}} > 0$) is seen for both integer fillings $\nu = 1$ and 2. (c),(d) Vertical cuts, respectively, from (a) and (b). The shades represent the standard deviation. Crossed Andreev reflection at $\nu = 2$ is undisturbed by bulk conductance and suppressed when the NbN superconductor turns normal at $T \sim 9$ K.

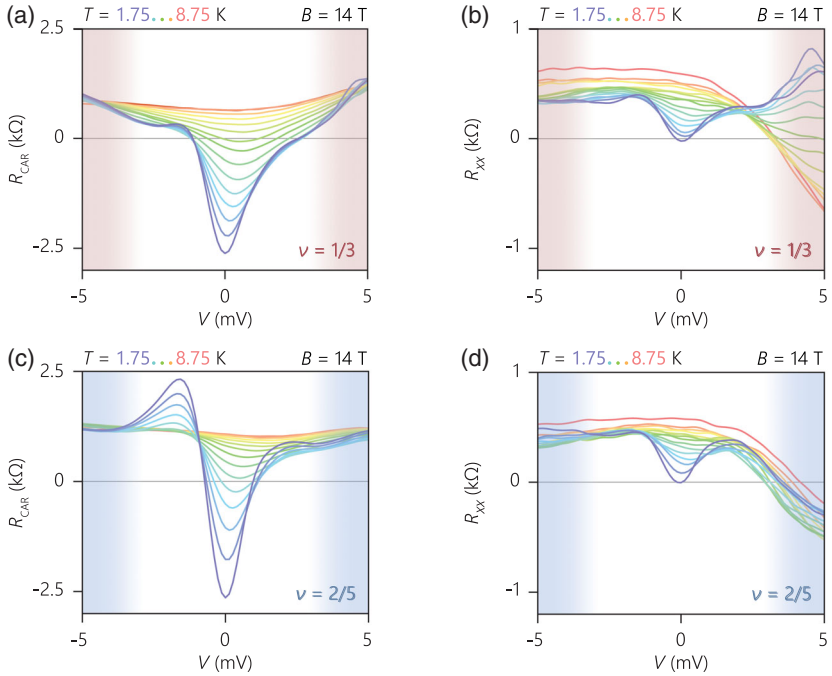

FIG. 15. Transport spectroscopy in device 1 showing R_{CAR} and R_{XX}. (a),(b) R_{CAR} and R_{XX} for $\nu = 1/3$ as a function of the incoming edge mode potential V (excitation) for different temperatures T. Crossed Andreev reflection ($R_{\mathrm{CAR}} < 0$) is limited to below $|eV| \sim 1$ meV. (c),(d) Same as (a) and (b) but for $\nu = 2/5$, which shows a V and T dependence similar to that for $\nu = 1/3$.

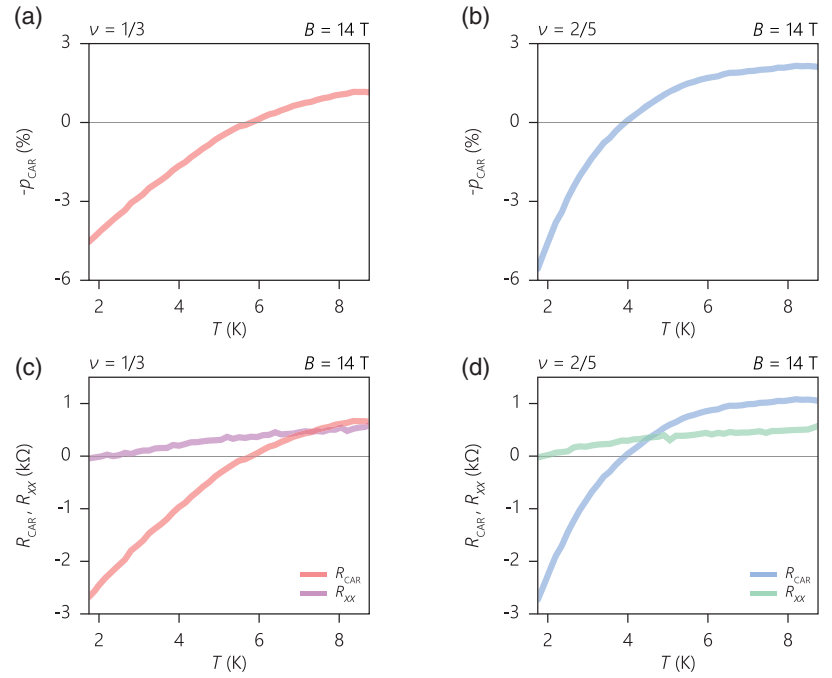

FIG. 16. Temperature dependence of crossed Andreev reflection at $\nu = 1/3$ and $2/5$ in device 1. (a) shows the CAR probability at $\nu = 1/3$, (b) shows that at $\nu = 2/5$. (c) and (d) respectively show R_{CAR} at $\nu = 1/3$ and $2/5$ together with the corresponding R_{XX}. Probability of crossed Andreev reflection in fillings $\nu = 1/3$ and $2/5$ is rapidly increasing with decreasing T down to the lowest temperature, at which bulk conductance vanishes ($R_{XX} \sim 0$). Data extracted from Figs. 5(a)–5(d).

ACKNOWLEDGMENTS

We thank Gil-Ho Lee, Yuval Oreg, Srijit Goswami, and Antonio Manesco for helpful discussions. Ö. G. acknowledges support by a Rubicon grant of the Netherlands Organization for Scientific Research (NWO). Y. R. and P. K. acknowledge support from DOE (DE-SC0012260) for measurement and analysis, and NSF (QII-TAQS MPS 1936263) for characterization. S. Y. L. and Y. H. L. acknowledge support from the Institute for Basic Science (IBS-R011-D1). H. S. and A. V. acknowledge support by the Simons Collaboration on Ultra-Quantum Matter, which is a grant from the Simons Foundation (651440, A. V.). J. Z. and A. Y. acknowledge support from DOE (DE-SC0019300) for device fabrication. A. Y. acknowledges funding by the NSF DMR-1708688. P. K. and A. Y. acknowledge experimental collaboration support from Science and Technology Center for Integrated Quantum Materials, NSF Grant No. DMR-1231319. K. W. and T. T. acknowledge support from the Elemental Strategy Initiative conducted by the MEXT, Japan (Grant No. JPMXP0112101001) and JSPS KAKENHI (Grants No. 19H05790 and No. JP20H00354). Nanofabrication was performed at the Center for Nanoscale Systems at Harvard, supported in part by a NSF NNIN Grant No. ECS-00335765.

Ö. G., Y. R., and P. K. conceived the idea and designed the project. P. K. supervised the project. Ö. G., Y. R., S. Y. L., and J. Z. fabricated the devices. H. S. and A. V. set up the theoretical model. Y. H. L. and A. Y. consulted on and helped in different stages of the fabrication process and analysis. Ö. G., Y. R., and J. Z. performed the measurements. Ö. G., Y. R., H. S., J. Z., A. Y., and P. K. wrote the paper with input from all authors.

APPENDIX A: EXPERIMENTAL METHODS

1. Assembly of the heterostructure

We assembled our five-layer graphite–hexagonal boron nitride (*h*BN)–single layer graphene–*h*BN–graphite van der Waals heterostructures with the standard dry transfer technique [51], using a polycarbonate- (PC) polydimethylsiloxane (PDMS) stamp. We exfoliated the flakes via thermal release tape onto (doped) Si substrates covered with 285-nm-thick SiO_2—the same substrate on which the devices were fabricated. To increase the size of the flakes we baked the substrates, the tape carrying bulk *h*BN and graphite still adhered, at 100 °C for 1 min on a hot plate before releasing the tape. After exfoliation we annealed the substrates with the flakes at high vacuum ($\sim 3 \times 10^{-7}$ mbar) and 350 °C for 20 min to remove the tape residues, ramping the temperature from 20 °C over 3 h. We did not perform these two heat treatments on single-layer graphene to avoid modifying its intrinsic properties. We determined the cleanness and thickness of the flakes by first optical and then atomic force microscopy. The graphite layers in our heterostructures were determined to be ~1.5–3 nm thick (5–10 layers) while the *h*BN layers were ~50 nm (top) and 90–100 nm (bottom), all confirmed to be atomically flat. We used a thicker bottom *h*BN to prevent an electrical connection between the bottom graphite and the overlapping superconductor (see Appendix A 2). After choosing suitable flakes, we assembled the heterostructure in a glovebox ($H_2O < 0.1$ ppm, $O_2 < 0.1$ ppm) to decrease contamination between the layers.

To make the stamp, we prepared a PC solution (8 wt %) and pipetted it onto a glass slide. We placed another glass slide on top of the solution and left the resulting film to cure in ambient conditions. We then placed a rectangular block (~8 × 5 mm) of PDMS (Gel-Pak) on a separate glass slide and transferred the PC film (with a larger area than that of the PDMS) on top. To ensure adhesion between the PC film and the glass slide we baked the stamp at 180 °C for 5 min, and then mounted the finished stamp on a dry transfer setup.

Before transferring flakes, we flattened the surface of the PC film by touching the stamp onto a bare substrate held by vacuum on a sample stage at 155 °C. After a cooldown period during which the PC film detached from the bare substrate, we replaced the substrate with the one containing the top graphite. The stamp was used to pick up the graphite at ~130 °C, followed by a cooldown until the stamp detached. We then used this top graphite to pick up the top *h*BN via van der Waals force. In this step, the top graphite approached the *h*BN extremely slowly at 150 °C–155 °C to minimize the formation of bubbles. We picked up this *h*BN, the graphene, and the bottom *h*BN with the same procedure described above. We then dropped the whole stack (graphite–*h*BN–graphene–*h*BN) from the stamp onto the bottom graphite at ~170 °C. Importantly, dropping the stack at this high temperature allowed us to push out the bubbles formed between the layers during assembly [52]. Finally, we released the PC film at 190 °C, ending the transfer process. We completed the assembly by removing polymer residues from the heterostructure, first leaving the chip in chloroform overnight and then annealing the heterostructure at high vacuum ($\sim 3 \times 10^{-7}$ mbar) and 350 °C for 30 min after a 3 h temperature ramp.

2. Nanofabrication

We defined the superconductor, normal leads, and the shape of the device via electron beam lithography followed by reactive ion etching (RIE). For RIE, we used a CHF_3, Ar, and O_2 gas mixture, whereas we excluded CHF_3 for the selective removal of the top graphite. Both the superconductor and the normal leads contact the graphene from its edge, and were deposited following RIE in one lithography step in which the etch mask also served as the deposition mask. For the superconductor, we first

selectively etched the top graphite that would otherwise surround the superconductor, leaving a ∼100 nm separation to avoid an electrical connection. In the subsequent lithography step, we deposited the superconductor after vertically etching the heterostructure beyond the graphene layer using an etch stop. This etch stop is based on the *ex situ* measured conductance of a test area of identical layer composition and leaves most of the bottom *h*BN unetched which insulates the superconductor from the bottom graphite. Unlike the superconductor, the normal leads do not overlap the top or bottom graphite, and instead connect to the fractional quantum Hall heterostructure through graphene that extends beyond both graphite layers (Fig. 6).

The normal leads are Cr/Pd/Au (2/7/150 nm), thermally evaporated on a rotating sample stage with ∼15° tilt. We deposited our superconductor in an AJA International UHV hybrid system (base pressure $\sim 10^{-7}$ Torr). The superconductor deposition started with electron beam evaporation of Ti (10 nm, with rotation and 15° tilt) immediately followed by dc magnetron sputtering of Nb/NbN (5/75 nm, without tilt) at a pressure of 3 mTorr and a power of 200 W using a Nb target. We deposited Nb in an Ar environment. For NbN we used an Ar/N_2 (50/6 sccm) gas mixture. This superconductor has a critical temperature $T_c \sim 12$ K at $B = 0$ T. An overview of the fabricated devices is given in Supplemental Material, Table S4.

3. Measurement

The parts of the graphene that extend beyond the top and bottom graphite, which connect the normal leads to the fractional quantum Hall heterostructure, were doped by using the substrate as a global gate. The top and bottom graphite layers were used as gates to control the charge carrier density in the fractional quantum Hall heterostructure. Device 1 used top graphite as the gate while the bottom graphite was grounded, whereas the opposite was the case for device 2 except in Fig. 4, where device 2 used top and bottom graphite simultaneously as gates.

We measured device 1 in a variable temperature inset (VTI) at $T \geq 1.75$ K and in a dilution refrigerator with its cold finger at $T = 15$ mK, and device 2 in a different VTI at $T \geq 1.6$ K. For the measurements in VTIs, we used a *RC* filter attached to the chip carrier, whereas the dilution refrigerator was equipped with *RC*, copper powder, and pi filters (*LCL* filter manufactured by Mini-Circuits) all thermalized to the cold finger. We reproduced our observations after every thermocycle for both our devices. Importantly, however, we were unable to measure crossed Andreev reflection without a filter.

We used the standard ac lock-in technique ($f = 17.77$ Hz) with an excitation current $I_{\mathrm{exc}} = 5$ or 10 nA for the VTI measurements and $I_{\mathrm{exc}} = 1$ or 5 nA for the dilution refrigerator measurements (ac circuit simulations of the device within the measurement circuit are provided in Refs. [35,53]). All presented measurements used a single source and the superconductor as the single drain. Because of the finite resistance (wiring and filters) between the superconductor and the breakout box at room temperature, V_{CAR} and V [Fig. 1(b)] were measured relative to the superconductor potential. Our superconductor coupled to the fractional quantum Hall edges branches out to four separate leads (Fig. 6). Two branch out immediately after leaving the heterostructure (one used as the drain, the other to monitor the potential), and the remaining two (left floating) after a narrow strip with identical dimensions as the one coupled to the fractional quantum Hall edges. This strip allowed for an independent test of our superconductor. An overview of the measured devices is given in Supplemental Material, Table S5 [35]. The data that support the findings of this study are available in Ref. [53].

APPENDIX B: THEORY

The inset of Fig. 2(b) (see also Fig. S1 in Supplemental Material [35]) shows the schematic of the vertically shrunk experimental system which satisfies $I_{\mathrm{exc}} = \nu \cdot e^2/h \cdot (V - V_{\mathrm{CAR}})$. A $p_{\mathrm{CAR}} = 1$ implies $R_{\mathrm{CAR}}/R_{XY} = -1/2$. In Supplemental Material [35], we present a low-energy theory of graphene in the presence of a strong out-of-plane B [54] (Fig. S2 in Supplemental Material) and compute crossed Andreev reflection for integer fillings. In the following, we first highlight the results of our integer quantum Hall theory analysis supporting our experimental findings, and then renormalization flow equations which describe CAR response in the FQH edge as the temperature is varied.

1. CAR in the integer quantum Hall state

We consider counterpropagating edge modes along either side of the superconductor [Fig. 2(b), inset, y axis is along the superconductor]. For reference, we show in Fig. S4 the armchair edge energy spectra in the absence and presence of the Dirac mass term, where we replace the superconducting region with vacuum (see Supplemental Material for details [35]). Without any (valley) symmetry breaking, the quantum Hall sequence is $\nu = 2, 4, 6, \ldots$. Adding the Dirac mass term modifies the sequence into $\nu = 1, 2, 4, \ldots$ with a spin and valley polarized $\nu = 1$. Turning on superconductivity yields Fig. 17, with the top panels for $\nu = 1$ and the bottom panels for $\nu = 2$. For any integer filling zero-energy band crossings are between particle-hole partners with identical spin polarization. Therefore, there is no direct mechanism for s-wave pairing (even for spin-unpolarized fillings such as $\nu = 2$). However, the large spin-orbit coupling in NbN superconductor provides a necessary ingredient for a spin-flip process allowing for a pairing between electrons with the same spin polarization. We account for spin-orbit coupling via [55]

$$h_{\mathrm{SO}} = \lambda_{\mathrm{SO}} \tau_z s_z \sigma_z + \lambda_{R,x} \tau_z s_y \sigma_x - \lambda_{R,y} s_x \sigma_y.$$

Because the induced pairing between the counterpropagating edge modes exponentially decays as a function of the

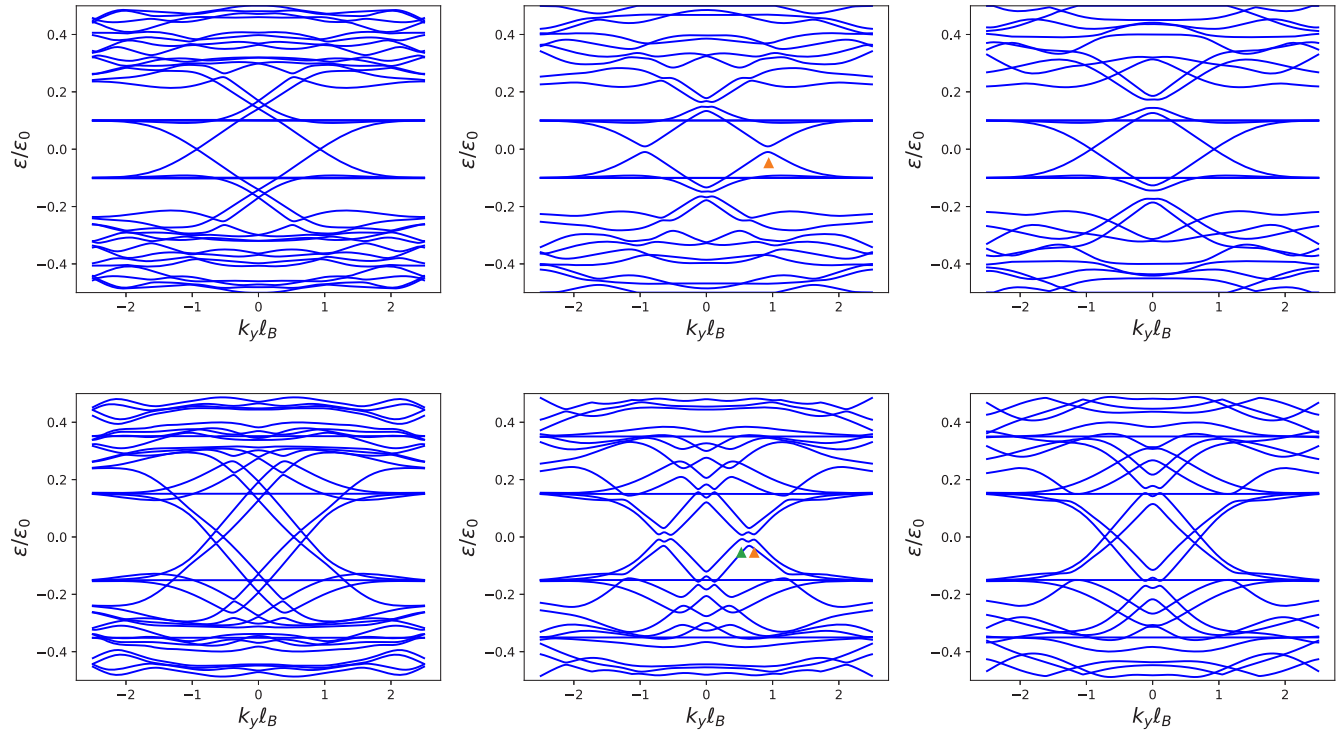

FIG. 17. Bogoliubov spectrum. Top row: $\nu = 1$ with $\mu_n = 0.3\varepsilon_0$. Bottom row: $\nu = 2$ with $\mu_n = 0.55\varepsilon_0$ (see the right-hand panel of Fig. S4 in Supplemental Material for the location of the chemical potential [35]). Left-hand column represents the case of a thick superconductor $W_s = 15l_B = 10\xi_0$. Middle and right-hand column correspond to a thin superconductor $W_s = 6l_B = 4\xi_0$. There is no energy gap in the thick regime, while there is a gap opening in the thin regime when spin-orbit coupling is present (middle column). For reference, we provide the right-hand column which has no spin-orbit coupling. In the other panels we set $\lambda_{Rx} = \varepsilon_0$. It is evident that either turning off the spin-orbit coupling or making the superconductor thick prevents the edge modes from hybridizing and leads to a gapless spectrum with propagating Andreev edge states along the QH-superconductor interface. For these simulations, the system parameters are set as follows: $\Delta_1 = 0.5\varepsilon_0$, $\Delta_2 = 0.6\varepsilon_0$, $m_s = 3\varepsilon_0$, $\mu_s = 8\varepsilon_0$, $\lambda_{Ry} = \lambda_{\mathrm{SO}} = 0$, $\lambda_{Rx} = \varepsilon_0$.

superconductor thickness, a gap does not open for a thick superconductor (left-hand panels). This is the experimental scenario in which Andreev edge states govern the transport [16,18,19,30,39,40]. Reducing the thickness of the superconductor hybridizes the edge modes along both sides of the superconductor and opens a gap in the Bogoliubov–de Gennes spectrum (middle panels). The band crossings and the resulting hybridization occur for each mode separately—each edge mode (for instance, spin-up and spin-down) experiences a similar induced pairing (gap opening) mechanism. The gap opening term is a spin-polarized pairing of the form $\psi_{Ls}\psi_{Rs}$, which originates from the combination of the spin-singlet pairing of the parent superconductor and spin-orbit coupling. Turning off spin-orbit coupling results in zero-energy band crossings remaining intact (right-hand panels). The degeneracy points (band crossings at finite energies) near $k_y = 0$ are lifted for a thin superconductor regardless of the presence of spin-orbit coupling. This is because those degeneracies open by either spin-singlet intraedge pairing or simply direct tunneling. Nevertheless, these processes do not play any role for the zero-energy band crossings between two spin-polarized modes since the former process does not open a gap in a spin-polarized channel and the latter is forbidden at finite k due to violating momentum conservation. This implies that $\nu = 2$ edge modes can be treated effectively as two copies of $\nu = 1$. Our numerical analysis confirms that the induced gaps within different edge modes are of the same order and decrease as the superconductor is made thicker (Fig. S5 in Supplemental Material [35]).

To study crossed Andreev reflection in a realistic experimental system we use an effective edge theory (see Supplemental Material for details [35]). We consider a disordered pairing potential,

$$V_{\mathrm{dis}} = \Delta_1(y)\tau_y\sigma_x s_y + \Delta_2(y)\tau_y\sigma_y,$$

which we vary over the minimum coherence length $\xi_0 \sim v_F/\Delta_m$. Here, both Δ_1 and Δ_2 are random variables drawn from a uniform distribution $[-\Delta_m, \Delta_m]$. (Note that here we suppress the complex phase of the pairing potential for simplicity. Our numerical results for disorder simulation do not exhibit qualitative change when we choose a complex pairing potential.) The resulting CAR is shown in Fig. 18. It is evident that in both the clean and the disordered case the zero-bias R_{CAR} is inversely proportional

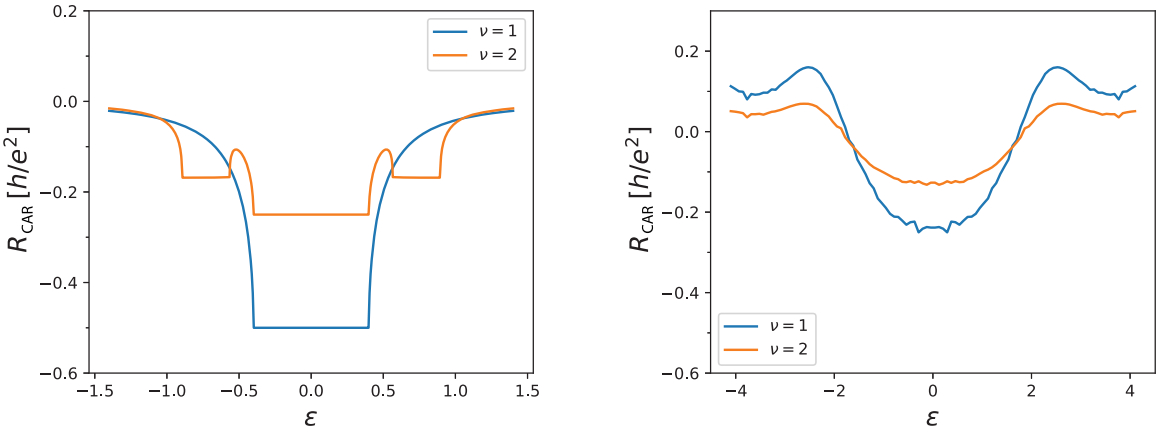

FIG. 18. Comparison of R_{CAR} for $\nu = 1$ and 2. Left is the ideal limit, right is the disordered pairing with $Z = 0.4$.

to the filling ν, consistent with the experiment. Notably, the experimental observation of CAR vanishing at finite energies can only be recovered in our calculation by introducing disorder which breaks translation symmetry and effectively produces direct tunneling terms. For the clean case, CAR remains consistently finite even at high energies. This implies that the pairing gap and disorder together determine the energy range of CAR. Finally, Fig. 19 compares the calculated CAR response with the experiment, qualitatively reproducing the observed

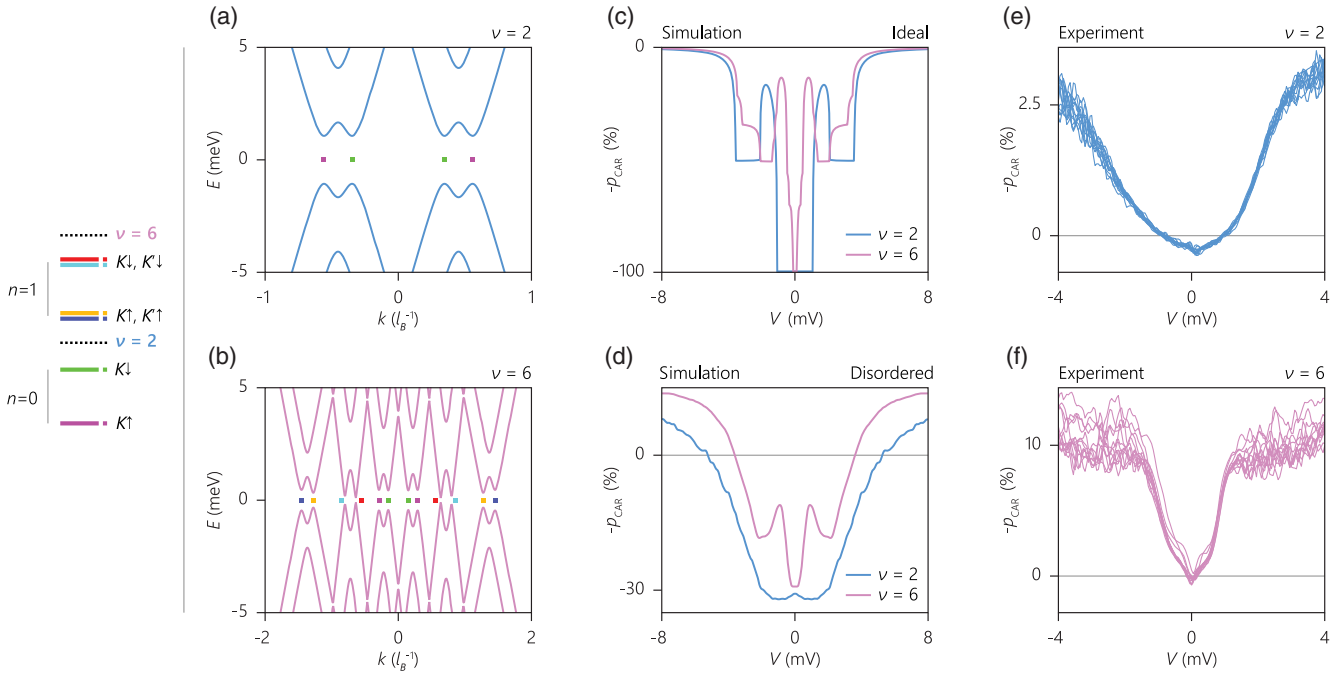

FIG. 19. Bogoliubov–de Gennes spectrum, calculated CAR response, and transport spectroscopy in device 1 for $\nu = 2$ and 6. (a),(b) Bogoliubov–de Gennes spectrum of $\nu = 2$ and 6 calculated using 2D simulations. Hybridization of the inner edge modes (those from lower Landau levels) is stronger due to their closer proximity to the superconductor, leading to larger gaps around k for which band crossings occur. Colored squares indicate the Landau levels whose edge modes hybridize. (c),(d) CAR response calculated using the effective edge theory in the ideal and the disordered case. For the clean case, CAR asymptotically vanishes at high energies. Including disorder limits the energy range for which $p_{CAR} > 0$. This implies that the pairing gap and disorder together determine the energy range of CAR in a realistic setup. We note that in the presence of disorder, p_{CAR} turns negative (i.e., R_{CAR} becomes positive) at a bias voltage much larger than the energy scale of Δ_{ind} due to direct tunneling processes dominating at higher energy. The parameters used in the effective theory are extracted from the 2D simulations for which the system parameters are the same as in Fig. 7 ($\mu_n = 1.2\varepsilon_0$ for $\nu = 6$). (e),(f) p_{CAR} at $\nu = 2$ and 6 as a function of the incoming edge mode potential V (excitation) for different gate voltages spanning the entire QH plateau region. CAR is limited to below $|eV| \sim 1$ meV for $\nu = 2$ and below $|eV| \sim 0.2$ meV for $\nu = 6$. (a) Same as in Fig. 2(d). (e),(f) Same as Figs. 2(e) and 2(f).

difference between $\nu = 2$ and 6. The larger energy range of CAR in $\nu = 2$ is due to its counterpropagating edge modes being closer to the superconductor than those of $\nu = 6$, which results in a stronger hybridization (larger Δ_{ind}). Apart from enabling direct tunneling, translation symmetry breaking also enables gap-opening superconducting pairing terms between counterpropagating edge modes of different Landau levels (for example, in $\nu = 2$ the inner edge mode can now pair with the counterpropagating outer edge mode), which is not possible for a disorder-free graphene-superconductor interface. This mechanism provides an additional *s*-wave contribution for fillings $\nu \geq 2$. (Note that for $\nu = 1$ no such *s*-wave term is present even with disorder.) However, such momentum-violating pairing terms hybridizing counterpropagating edge modes from different Landau levels are likely not dominant in the experimental system because no strong filling dependence is observed, particularly for $\nu = 1$ versus larger fillings $\nu \geq 2$.

2. CAR in the fractional quantum Hall state

Now we turn to the FQH state, which requires different approaches from the integer QH CAR discussed above. For simplicity, we shall consider only the $\nu = 1/m$ Laughlin states (with odd m), where the edge theory is single component. The system is described by two chiral edge modes near top and bottom of the sample:

$$\mathcal{L}_{\text{edge}} = \frac{1}{4\pi\nu}\int dy[\partial_t\phi_L\partial_y\phi_L - V\partial_y\phi_L\partial_y\phi_L] + \frac{1}{4\pi\nu}\int dy[-\partial_t\phi_R\partial_y\phi_R - V\partial_y\phi_R\partial_y\phi_R],$$

where

$$[\phi_{L,R}(y_1), \phi_{L,R}(y_2)] = \mp\, i\frac{\pi}{m}\text{sgn}(y_1 - y_2),$$
$$[\phi_L(y_1), \phi_R(y_2)] = i\frac{\pi}{m}.$$

$\phi_{L,R}$ are chiral bosons [56,57]. Using this formulation, the electric charge density associated with ϕ_α is given by

$$\rho_\alpha = \frac{1}{2\pi}\partial_y\phi_\alpha,$$

and the Ith electron operator is described by the vertex operator,

$$\Psi_{e,L/R} = e^{i\nu^{-1}\phi_{L/R}}.$$

In the right half of the system [recall Fig. 2(b), inset] the two edge modes are decoupled. In the left half, the two edge modes are coupled via the following induced pairing term:

$$\mathcal{L}_{\text{pairing}} = \Delta\int_0^\infty dx\, \cos\nu^{-1}(\phi_L + \phi_R).$$

Note that we drop the Klein factor since it commutes with other terms in the Hamiltonian. The bare scaling dimension of this term is $1 - \nu^{-1}$. However, we work in the strong coupling limit $\Delta \to \infty$. The ground state of the $x > 0$ region is obtained by pinning the field $\nu^{-1}(\phi_L + \phi_R) = 2\pi n$, where $n = 0, 1, 2, \ldots, \nu^{-1} - 1$. This in turn implies not only $e^{i\nu^{-1}(\phi_L+\phi_R)} \neq 0$ but also $e^{i(\phi_L+\phi_R)} \neq 0$; that is, we get a condensate of quasiparticle and quasihole pairs. The scattering of a (quasi)particle impinging on the $x > 0$ region from the left region can be addressed by the following two processes:

(1) coherent conversion of a right-moving quasielectron to a left-moving quasihole, which is described by the following term

$$\Gamma_{qp}\int dy\delta(y - 0^-)e^{i(\phi_L+\phi_R)} + \text{H.c.}$$

(2) coherent conversion of a right-moving electron to a left-moving hole, which is described by the following term:

$$\Gamma_{eh}\int dy\delta(y - 0^-)e^{i\nu^{-1}(\phi_L+\phi_R)} + \text{H.c.}$$

The latter process requires electron bunching before going through the superconductor. The scaling dimensions of the two processes are given by ν and ν^{-1}, respectively. Hence, the tunneling amplitudes obey the renormalization flow equations,

$$\frac{d\Gamma_{qp}}{dl} = (1 - \nu),$$
$$\frac{d\Gamma_{eh}}{dl} = (1 - \nu^{-1}),$$

which implies that in the infrared limit (low energy), for $\nu < 1$, Γ_{qp} is relevant while Γ_{eh} is irrelevant. Now, we compare experimental consequences of both processes (Fig. 20).

(1) Γ_{qp}: Since this term is relevant, it drives the system to a strong coupling limit fixed point $\Gamma_{qp} \to \infty$ in the low-energy limit. So, we expect that at low temperatures there is a constant CAR response proportional to $|\Gamma_{qp}|^2$ and it gradually decreases as $T^{2\nu-2}$ when the temperature is increased or as $V^{2\nu-2}$ when a bias voltage is applied.

(2) Γ_{eh}: Since this term is irrelevant, at zero temperature the system in a weak coupling limit $\Gamma_{eh} \to 0$ and there is no CAR response. We expect that as we increase the temperature or apply a bias voltage, the CAR response increases as $T^{2\nu^{-1}-2}$ or $V^{2\nu^{-1}-2}$, respectively.

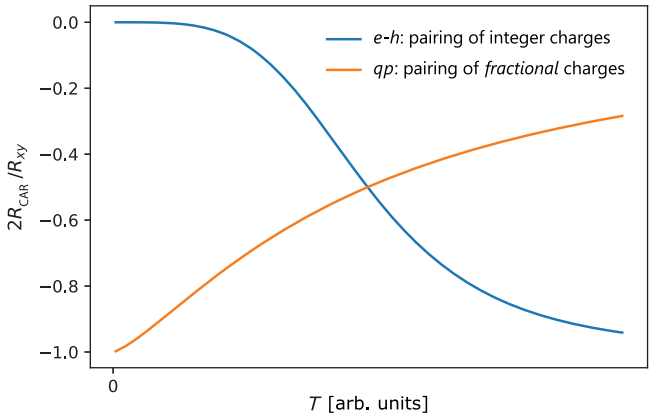

FIG. 20. Temperature dependence of R_{CAR} in a FQH edge mode. R_{CAR} at the edge of Laughlin states shows different temperature dependences for two separate pairing scenarios. In one scenario, pairing occurs between fractional charges; that is, crossed Andreev reflection converts fractionally charged quasiparticles to fractionally charged quasiholes. This mechanism results in an increasing $|R_{\mathrm{CAR}}|$ with decreasing temperature T. Such T dependence is not present in the alternative scenario where pairing occurs between integer charges which are formed by bunched fractional charges. Here, crossed Andreev reflection converts particles with integer charge to holes with integer charge. In this case, R_{CAR} vanishes at $T = 0$ because in a FQH state integer charges are composed of excitations which are nonexistent at zero T. The probability to form integer charges is then proportional to a large power of T. Both these scenarios are specific to the FQH state. No temperature dependence is expected for integer quantum Hall edge modes. CAR of fractional charges (first scenario) implies addition of fractional charges to a fractional topological superconductor hosting parafermions—a mechanism similar to Majoranas allowing for transport of single charges in a topological superconductor, which is not possible in a conventional superconductor. A similar mechanism analogous to CAR of fractional charges occurs in a quantum point contact (QPC) separating two FQH state regions. Here, fractional charges first tunnel through the QPC [58,59], and then are drained from a metal electrode which does not host fractional excitations. In this analogy, the tunneling of fractional charges through a QPC is similar to our CAR of fractional charges. The metal electrode draining the edge modes after a QPC is similar to our conventional superconductor away from the proximitized region.

Given that the experimental data as a function of temperature show an initial plateau and gradual increase as T is decreased, we conclude that Γ_{qp} is the dominant term governing the CAR response. Note that this scaling analysis provides a qualitative picture. Further quantitative discussion on FQH CAR requires many-body simulation of the FQH states.

[1] A. Y. Kitaev, *Fault-Tolerant Quantum Computation by Anyons*, Ann. Phys. (Amsterdam) **303**, 2 (2003).
[2] N. Read and D. Green, *Paired States of Fermions in Two Dimensions with Breaking of Parity and Time-Reversal Symmetries and the Fractional Quantum Hall Effect*, Phys. Rev. B **61**, 10267 (2000).
[3] A. Y. Kitaev, *Unpaired Majorana Fermions in Quantum Wires*, Phys. Usp. **44**, 131 (2001).
[4] C. Nayak, S. H. Simon, A. Stern, M. Freedman, and S. Das Sarma, *Non-Abelian Anyons and Topological Quantum Computation*, Rev. Mod. Phys. **80**, 1083 (2008).
[5] L. Fu and C. L. Kane, *Superconducting Proximity Effect and Majorana Fermions at the Surface of a Topological Insulator*, Phys. Rev. Lett. **100**, 096407 (2008).
[6] S. Hart, H. Ren, T. Wagner, P. Leubner, M. Mühlbauer, C. Brüne, H. Buhmann, L. W. Molenkamp, and A. Yacoby, *Induced Superconductivity in the Quantum Spin Hall Edge*, Nat. Phys. **10**, 638 (2014).
[7] J. Wiedenmann *et al.*, 4π*-Periodic Josephson Supercurrent in HgTe-Based Topological Josephson Junctions*, Nat. Commun. **7**, 10303 (2016).
[8] H.-H. Sun, K.-W. Zhang, L.-H. Hu, C. Li, G.-Y. Wang, H.-Y. Ma, Z.-A. Xu, C.-L. Gao, D.-D. Guan, Y.-Y. Li *et al.*, *Majorana Zero Mode Detected with Spin Selective Andreev Reflection in the Vortex of a Topological Superconductor*, Phys. Rev. Lett. **116**, 257003 (2016).
[9] V. Mourik, K. Zuo, S. M. Frolov, S. R. Plissard, E. P. A. M. Bakkers, and L. P. Kouwenhoven, *Signatures of Majorana Fermions in Hybrid Superconductor-Semiconductor Nanowire Devices*, Science **336**, 1003 (2012).
[10] L. P. Rokhinson, X. Liu, and J. K. Furdyna, *The Fractional a.c. Josephson Effect in a Semiconductor–Superconductor Nanowire as a Signature of Majorana Particles*, Nat. Phys. **8**, 795 (2012).
[11] A. Das, Y. Ronen, Y. Most, Y. Oreg, M. Heiblum, and H. Shtrikman, *Zero-Bias Peaks and Splitting in an Al–InAs Nanowire Topological Superconductor as a Signature of Majorana Fermions*, Nat. Phys. **8**, 887 (2012).
[12] M. T. Deng, C. L. Yu, G. Y. Huang, M. Larsson, P. Caroff, and H. Q. Xu, *Anomalous Zero-Bias Conductance Peak in a Nb–InSb Nanowire–Nb Hybrid Device*, Nano Lett. **12**, 6414 (2012).
[13] A. D. K. Finck, D. J. Van Harlingen, P. K. Mohseni, K. Jung, and X. Li, *Anomalous Modulation of a Zero-Bias Peak in a Hybrid Nanowire-Superconductor Device*, Phys. Rev. Lett. **110**, 126406 (2013).
[14] H. O. H. Churchill, V. Fatemi, K. Grove-Rasmussen, M. T. Deng, P. Caroff, H. Q. Xu, and C. M. Marcus, *Superconductor-Nanowire Devices from Tunneling to the Multichannel Regime: Zero-Bias Oscillations and Magnetoconductance Crossover*, Phys. Rev. B **87**, 241401(R) (2013).
[15] S. Nadj-Perge, I. K. Drozdov, J. Li, H. Chen, S. Jeon, J. Seo, A. H. MacDonald, B. A. Bernevig, and A. Yazdani, *Observation of Majorana Fermions in Ferromagnetic Atomic Chains on a Superconductor*, Science **346**, 602 (2014).
[16] F. Amet *et al.*, *Supercurrent in the Quantum Hall Regime*, Science **352**, 966 (2016).
[17] G.-H. Lee, K.-F. Huang, D. K. Efetov, D. S. Wei, S. Hart, T. Taniguchi, K. Watanabe, A. Yacoby, and P. Kim, *Inducing Superconducting Correlation in Quantum Hall Edge States*, Nat. Phys. **13**, 693 (2017).
[18] L. Zhao *et al.*, *Interference of Chiral Andreev Edge States*, Nat. Phys. **16**, 862 (2020).

[19] M. Hatefipour *et al.*, *Induced Superconducting Pairing in Integer Quantum Hall Edge States*, arXiv:2108.08899.

[20] N. Read and E. Rezayi, *Beyond Paired Quantum Hall States: Parafermions and Incompressible States in the First Excited Landau Level*, Phys. Rev. B **59**, 8084 (1999).

[21] R. S. K. Mong *et al.*, *Universal Topological Quantum Computation from a Superconductor-Abelian Quantum Hall Heterostructure*, Phys. Rev. X **4**, 011036 (2014).

[22] J. Alicea and P. Fendley, *Topological Phases with Parafermions: Theory and Blueprints*, Annu. Rev. Condens. Matter Phys. **7**, 119 (2016).

[23] A. Vaezi and M. Barkeshli, *Fibonacci Anyons from Abelian Bilayer Quantum Hall States*, Phys. Rev. Lett. **113**, 236804 (2014).

[24] A. Vaezi, *Superconducting Analogue of the Parafermion Fractional Quantum Hall States*, Phys. Rev. X **4**, 031009 (2014).

[25] D. J. Clarke, J. Alicea, and K. Shtengel, *Exotic Non-Abelian Anyons from Conventional Fractional Quantum Hall States*, Nat. Commun. **4**, 1348 (2013).

[26] N. H. Lindner, E. Berg, G. Refael, and A. Stern, *Fractionalizing Majorana Fermions: Non-Abelian Statistics on the Edges of Abelian Quantum Hall States*, Phys. Rev. X **2**, 041002 (2012).

[27] M. Cheng, *Superconducting Proximity Effect on the Edge of Fractional Topological Insulators*, Phys. Rev. B **86**, 195126 (2012).

[28] A. Vaezi, *Fractional Topological Superconductor with Fractionalized Majorana Fermions*, Phys. Rev. B **87**, 035132 (2013).

[29] M. Barkeshli and X.-L. Qi, *Synthetic Topological Qubits in Conventional Bilayer Quantum Hall Systems*, Phys. Rev. X **4**, 041035 (2014).

[30] P. Rickhaus, M. Weiss, L. Marot, and C. Schönenberger, *Quantum Hall Effect in Graphene with Superconducting Electrodes*, Nano Lett. **12**, 1942 (2012).

[31] Z. Wan, A. Kazakov, M. J. Manfra, L. N. Pfeiffer, K. W. West, and L. P. Rokhinson, *Induced Superconductivity in High-Mobility Two-Dimensional Electron Gas in Gallium Arsenide Heterostructures*, Nat. Commun. **6**, 7426 (2015).

[32] A. A. Zibrov, C. Kometter, H. Zhou, E. M. Spanton, T. Taniguchi, K. Watanabe, M. P. Zaletel, and A. F. Young, *Tunable Interacting Composite Fermion Phases in a Half-Filled Bilayer-Graphene Landau Level*, Nature (London) **549**, 360 (2017).

[33] J. I. A. Li, C. Tan, S. Chen, Y. Zeng, T. Taniguchi, K. Watanabe, J. Hone, and C. R. Dean, *Even-Denominator Fractional Quantum Hall States in Bilayer Grapheme*, Science **358**, 648 (2017).

[34] D. J. Clarke, J. Alicea, and K. Shtengel, *Exotic Circuit Elements from Zero-Modes in Hybrid Superconductor–Quantum-Hall Systems*, Nat. Phys. **10**, 877 (2014).

[35] See Supplemental Material at http://link.aps.org/supplemental/10.1103/PhysRevX.12.021057 for the theory model (Supplement I), ac circuit simulations of the measurement circuit (Supplement II), expected energy scales (Table S3), line traces of R_{CAR} from Fig. 3(c) plotted along with their corresponding R_{XX} (Fig. S10), color plots in linear color scale (Figs. S11–S15), figures which use low-pass smoothing next to their unsmoothed versions (Figs. S16–S23), data shown in Fig. 1(f) focusing on $\nu = 1/3$ (Fig. S24), and an overview of fabricated and measured devices (Tables S4 and S5).

[36] K. T. Law, P. A. Lee, and T. K. Ng, *Majorana Fermion Induced Resonant Andreev Reflection*, Phys. Rev. Lett. **103**, 237001 (2009).

[37] H. Pan and S. Das Sarma, *Physical Mechanisms for Zero-Bias Conductance Peaks in Majorana Nanowires*, Phys. Rev. Research **2**, 013377 (2020).

[38] A. Marguerite, J. Birkbeck, A. Aharon-Steinberg, D. Halbertal, K. Bagani, I. Marcus, Y. Myasoedov, A. K. Geim, D. J. Perello, and E. Zeldov, *Imaging Work and Dissipation in the Quantum Hall State in Grapheme*, Nature (London) **575**, 628 (2019).

[39] Z. Hou, Y. Xing, A.-M. Guo, and Q.-F. Sun, *Crossed Andreev Effects in Two-Dimensional Quantum Hall Systems*, Phys. Rev. B **94**, 064516 (2016).

[40] A. R. L. Manesco, I. M. Flór, C.-X. Liu, and A. R. Akhmerov, *Mechanisms of Andreev Reflection in Quantum Hall Grapheme*, arXiv:2103.06722.

[41] G. Nanda, J. L. Aguilera-Servin, P. Rakyta, A. Kormányos, R. Kleiner, D. Koelle, K. Watanabe, T. Taniguchi, L. M. K. Vandersypen, and S. Goswami, *Current-Phase Relation of Ballistic Graphene Josephson Junctions*, Nano Lett. **17**, 3396 (2017).

[42] A. H. MacDonald, *Edge States in the Fractional-Quantum-Hall-Effect Regime*, Phys. Rev. Lett. **64**, 220 (1990).

[43] C. L. Kane, M. P. Fisher, and J. Polchinski, *Randomness at the Edge: Theory of Quantum Hall Transport at Filling* $\nu = 2/3$, Phys. Rev. Lett. **72**, 4129 (1994).

[44] M. Hashisaka, T. Jonckheere, T. Akiho, S. Sasaki, J. Rech, T. Martin, and K. Muraki, *Andreev Reflection of Fractional Quantum Hall Quasiparticles*, Nat. Commun. **12**, 2794 (2021).

[45] D. S. Wei, T. van der Sar, S. H. Lee, K. Watanabe, T. Taniguchi, B. I. Halperin, and A. Yacoby, *Electrical Generation and Detection of Spin Waves in a Quantum Hall Ferromagnet*, Science **362**, 229 (2018).

[46] H. Zhou, H. Polshyn, T. Taniguchi, K. Watanabe, and A. F. Young, *Solids of Quantum Hall Skyrmions in Graphene*, Nat. Phys. **16**, 154 (2020).

[47] M. Barkeshli, Y. Oreg, and X.-L. Qi, *Experimental Proposal to Detect Topological Ground State Degeneracy*, arXiv:1401.3750.

[48] N. Schiller, E. Cornfeld, E. Berg, and Y. Oreg, *Predicted Signatures of Topological Superconductivity and Parafermion Zero Modes in Fractional Quantum Hall Edges*, Phys. Rev. Research **2**, 023296 (2020).

[49] A. B. Michelsen, T. L. Schmidt, and E. G. Idrisov, *Current Correlations of Cooper-Pair Tunneling into a Quantum Hall System*, Phys. Rev. B **102**, 125402 (2020).

[50] A. E. Svetogorov, D. Loss, and J. Klinovaja, *Insulating Regime of an Underdamped Current-Biased Josephson Junction Supporting* Z_3 *and* Z_4 *Parafermions*, Phys. Rev. B **103**, L180505 (2021).

[51] L. Wang *et al.*, *One-Dimensional Electrical Contact to a Two-Dimensional Material*, Science **342**, 614 (2013).

[52] D. G. Purdie, N. M. Pugno, T. Taniguchi, K. Watanabe, A. C. Ferrari, and A. Lombardo, *Cleaning Interfaces in*

Layered Materials Heterostructures, Nat. Commun. **9**, 5387 (2018).

[53] Measurement data, data processing and figure generating scripts of this study are available at 10.5281/zenodo.6586602.

[54] D. A. Abanin, P. A. Lee, and L. S. Levitov, *Charge and Spin Transport at the Quantum Hall Edge of Graphene*, Solid State Commun. **143**, 77 (2007).

[55] H. Min, J. E. Hill, N. A. Sinitsyn, B. R. Sahu, L. Kleinman, and A. H. MacDonald, *Intrinsic and Rashba Spin-Orbit Interactions in Graphene Sheets*, Phys. Rev. B **74**, 165310 (2006).

[56] X.-G. Wen, *Chiral Luttinger Liquid and the Edge Excitations in the Fractional Quantum Hall States*, Phys. Rev. B **41**, 12838 (1990).

[57] X.-G. Wen, *Theory of the Edge States in Fractional Quantum Hall Effects*, Int. J. Mod. Phys. B **06**, 1711 (1992).

[58] L. Saminadayar, D. C. Glattli, Y. Jin, and B. Etienne, *Observation of the $e/3$ Fractionally Charged Laughlin Quasiparticles*, Phys. Rev. Lett. **79**, 2526 (1997).

[59] R. de-Picciotto, M. Reznikov, M. Heiblum, V. Umansky, G. Bunin, and D. Mahalu, *Direct Observation of a Fractional Charge*, Nature (London) **389**, 162 (1997).